

Cryptic developmental events determine medulloblastoma radiosensitivity and cellular heterogeneity without altering transcriptomic profile.

Daniel Shiloh Malawsky

UNC

Seth Weir

UNC

Jennifer Ocasio

UNC

Ben Babcock

UNC <https://orcid.org/0000-0002-2902-8045>

Taylor Dismuke

UNC

Kirk Wilhelmsen

UNC <https://orcid.org/0000-0002-4432-8302>

Timothy (R.) Gershon (✉ gershont@neurology.unc.edu)

UNC <https://orcid.org/0000-0001-7034-6400>

Article

Keywords:

Posted Date: August 7th, 2020

DOI: <https://doi.org/10.21203/rs.3.rs-50396/v1>

License:  This work is licensed under a Creative Commons Attribution 4.0 International License.

[Read Full License](#)

Version of Record: A version of this preprint was published at Communications Biology on May 21st, 2021. See the published version at <https://doi.org/10.1038/s42003-021-02099-w>.

Abstract

Patients with medulloblastoma are typically treated with a narrow range of therapies, but may experience widely divergent outcomes; 80-90% become long-term survivors while 20% develop incurable recurrence. Transcriptomic profiling has identified four subgroups with different recurrence risks, but outcomes remain variable for individual patients within each subgroup. To gain new insight into why patients with similar-appearing tumors have variable outcomes, we examined how the timing of tumor initiation effects medulloblastomas triggered by a single, common driver mutation. We genetically-engineered mice to express an oncogenic Smo allele starting early in development in the broad lineage of neural stem cells, or later, in the more committed lineage of cerebellar granule neuron progenitors. Both groups developed medulloblastomas and no other tumors. We compared medulloblastoma progression, response to therapy, gene expression profile and cellular heterogeneity, determined by single cell transcriptomic analysis (scRNA-seq). The average transcriptomic profiles of the tumors were similar. However, stem cell-triggered medulloblastomas progressed faster, contained more OLIG2-expressing tumor stem cells, and consistently showed radioresistance. In contrast, progenitor-triggered MBs progressed slower, lost stem cell character over time and were radiosensitive. Progenitor-triggered medulloblastomas also contained more diverse stromal populations, including tumor-associated macrophages, indicating that the timing of oncogenesis affected the subsequent interactions between the tumor and microenvironment. Our findings show that developmental events in tumorigenesis may be impossible to infer from transcriptomic profile, but while remaining cryptic can nevertheless influence tumor composition and the outcome of therapy. Precise understanding of medulloblastoma pathogenesis and prognosis requires supplementing transcriptomic data with biomarkers of cellular heterogeneity.

Introduction

Medulloblastoma, the most common malignant pediatric brain tumor, is frequently curable with surgery, radiation and chemotherapy. However, not all patients respond to therapy, and individual patients face a significant risk of treatment failure. Transcriptomic studies have identified four major subgroups of medulloblastoma: WNT, SHH, group 3 and group 4 (1). Each subgroup has a different prognosis, but within each subgroup, outcomes are heterogeneous (2). The factors that determine the variable outcomes for patients with similar-appearing medulloblastomas are unclear. We tested the possibility that different outcomes of medulloblastoma therapy can be determined by developmental events that are cryptic at the time of presentation.

SHH-subgroup medulloblastomas are grouped together because they show similar patterns of gene expression in bulk transcriptomic studies, indicating SHH pathway activation. Despite sharing a common oncogenic pathway, patients with SHH-subgroup medulloblastomas show different responses to treatment, with ~ 20% developing incurable recurrence. It is not clear whether differences in outcome are stochastic or driven by determinants that remain to be identified. Age of onset, however, is a factor that clearly influences prognosis within each subgroup (2), suggesting a potential effect of developmental timing on tumor behavior.

Prior studies in genetically-engineered mice show that cerebellar granule cell progenitors (CGNPs) are proximal cells of origin for SHH-driven medulloblastoma (3, 4). CGNPs are a population of SHH-responsive, committed neural progenitors that derive from the rhombic lip, migrate to the external granule layer (EGL) of the cerebellum, and then proliferate rapidly in response to SHH ligand secreted by the Purkinje neurons (5, 6). CGNPs proliferate in the first two weeks of life in mice, or the first year of life in humans, to generate the cerebellar granule neurons (CGNs) the largest neuronal population in the brain (7). Mutations that hyperactivate SHH signaling in CGNPs cause familial medulloblastoma in humans and recapitulate medulloblastoma formation in mice, providing genetically faithful primary tumor models (3, 4, 8).

Importantly, CGNPs are not a homogeneous population. While the EGL is predominantly populated by ATOH1 (AKA MATH1)-expressing progenitors, a small subset of NESTIN+/ ATOH1- cells reside in the EGL (9). These EGL cells are typically quiescent *in vivo* but proliferate in response to SHH pathway activation and can give rise to SHH-driven medulloblastoma (9). Moreover, the ATOH1+ cells of the EGL comprise different subsets (10, 11), including a transient subpopulation that express the stem cell marker SOX2 and may be particularly vulnerable to SHH-driven tumorigenesis (11).

The developmental origins of medulloblastoma can be analyzed by pairing different Cre drivers with conditional mutations of the SHH receptor components *Ptc* and *Smo* directing SHH hyperactivation to broad lineages that include CGNPs or more narrow lineages within the CGNP population. For example, *Gfap-Cre* targets a lineage of neuroglial stem cells throughout the brain that includes both ATOH1+ CGNPs and NESTIN+/ ATOH1- cells of the EGL (12, 13). *Math1-Cre*, in contrast, targets the ATOH1-expressing CGNPs (14-16), including the SOX2+ subset (11). A prior study compared the effects of deleting *Ptc* either in neural stem cells in *Gfap-Cre*

/Ptcfl/fl mice or in CGNPs in *Math1-Cre/PtcloxP/loxP* mice (17). Both genotypes developed medulloblastoma with 100% penetrance. In *Gfap-Cre /Ptcfl/fl* where SHH was hyperactivated throughout the brain, tumors developed only in the cerebellum. Similarly, inducing a Cre-dependent, constitutively active allele of *Smo* (*SmoM2*) in either stem cells or CGNPs, using respectively *Gfap-Cre* or *Math1-Cre*, resulted in medulloblastoma with 100% penetrance (18). These studies show that the EGL population is uniquely competent to undergo SHH-mediated tumorigenesis, and that cells with hyperactivation of SHH signaling prior to the formation of the EGL must advance along the CGN developmental trajectory by migrating to the cerebellar surface before giving rise to tumors (17, 18).

Medulloblastomas initiated by *Gfap-Cre* in stem cells progressed faster, as medulloblastomas initiated by *Math1-Cre*, producing a shorter EFS despite occurring in the same location and showing similar pathology and gene expression profile (17, 18). In another comparison of medulloblastomas initiated by conditional activation of *SmoM2* either prenatally, using *Gfap-Cre*, or postnatally, using tamoxifen-inducible *Math1-CreER*, the resulting tumors were histologically and molecularly indistinguishable, but showed different propensities for anchorage-independent growth *in vitro* (19). Thus, SHH-driven

medulloblastomas triggered in stem or progenitor cells have shown both overall similarities and specific differences.

The different survival times when tumors are triggered with *Gfap-Cre* or *Math1-Cre* suggest that the timing of the oncogenic event can act as a cryptic factor that produces clinically relevant effects that persist throughout the generations of tumor cells. We tested the clinical relevance of this possibility by comparing the responses to therapy of medulloblastomas initiated in either stem cells or neural progenitors, and by subjecting both types of tumors to scRNA-seq analysis. We show that timing of tumor initiation within the lineage trajectory of GFAP+ stem cells to ATOH1+ progenitors influences the cellular heterogeneity within the resulting tumors, without detectably altering average gene expression profiles, producing tumors that appear similar but contain divergent subpopulations with different tumor-stromal interactions and treatment responses.

Results

Similar pathology and gene expression in medulloblastomas from progenitors or stem cells

To initiate an oncogenic stimulus in CGNPs, we bred *SmoM2* mice with *Math1-Cre* mice to generate *Math1-Cre/SmoM2* (*M-Smo*) pups. To initiate an oncogenic stimulus earlier in brain development in pluripotent stem cells that give rise to CGNPs, we bred *SmoM2* mice to *Gfap-Cre* mice to generate *Gfap-Cre/SmoM2* (*G-Smo*) pups. Both *M-Smo* and *G-Smo* genotypes developed cerebellar tumors with 100% frequency and all tumors showed the small, round blue cell morphology typical of medulloblastoma and tendency to invade adjacent brain (Fig. 1a).

Microarray comparison of gene expression in samples from *M-Smo* and *G-Smo* tumors showed similar transcriptomic profiles with 64/41349 probes sets detecting statistically significant signals, representing 33 identified transcripts (Supplementary Table 1). One of these differentially expressed transcripts, *Protamine 1* (*Prm1*) was included within the *Gfap-Cre* transgene, and thus expected to be differentially detected. Finding differential *Prm1* provided an internal validation of the assay, while finding only 32 other differential transcripts demonstrated the high similarity between the tumors. Similarly, the same work flow applied to the previously published microarray datasets from *G-Smo* and *M-Smo* tumors (18) identified 66 out of 45105 probe sets, representing 54 differentially detected transcripts (Supplementary Table 2). Only 1 gene was differentially expressed in both studies. Both microarray comparisons demonstrated highly similar average gene expression profiles of *G-Smo* and *M-Smo* tumors, with minimal consistently observed differences.

Different, clinically-relevant behaviors of medulloblastomas from progenitors or stem cells

In contrast to the similarity in pathology and average gene expression of *G-Smo* and *M-Smo* tumors, we noted marked differences in the clinically relevant parameters of survival time and response to therapy. As in the prior study (18), the survival times of untreated *G-Smo* mice were typically shorter than those of *M-Smo* mice (Fig 1b). Moreover, while *M-Smo* mice showed significantly improved survival after radiation

therapy (xRT), consistent with our prior studies (20), xRT did not extend the survival of *G-Smo* mice (Fig. 1c,d). The prognosis of *G-Smo* and *M-Smo* mice was therefore markedly different, despite their common oncogenic driver, tumor pathology and similarity in bulk transcriptomic studies.

scRNA-seq identifies difference between medulloblastomas from progenitors or stem cells

To examine the differences between *G-Smo* and *M-Smo* tumors with cellular resolution, we analyzed both tumor types using scRNA-seq. Transcriptomic analysis at single cell resolution allowed us to examine tumor sub-populations that might be overlooked in bulk transcriptomic studies. We harvested medulloblastomas from 5 *M-Smo* and 6 *G-Smo* at P15, dissociated the tumors and subjected the cells to bead-based Drop-seq analysis, as previously described (10). Putative cells identified by bead-specific barcodes were subjected to exclusion criteria described in Methods, to address the common problems of gene drop out, unintentional cell-cell multiplexing and premature cell lysis (21, 22). 5930 out of 11984 putative *M-Smo* cells, and 8699 out of 16489 *G-Smo* cells met criteria and were included in the analysis. To compare the two genotypes at similar sequencing depths, we randomly downsampled the *G-Smo* transcript counts to 60% of the original depth, as recommended in prior studies (23).

We subjected the scRNA-seq data from *M-Smo* and *G-Smo* tumors to a single principle component analysis (PCA) followed by Louvain clustering, as in our prior studies comparing *M-Smo* tumors with and without treatment (10). We identified 17 principle components that described >78% of the variance and used UMAP to place cells in a 2-dimensional space according to their distances in PCA space, with Louvain clusters color-coded (Fig. 2a). We noted that cells in the same clusters localized close together in the UMAP, supporting the validity of the cluster assignments. To determine the biological relevance of the clusters, we generated cluster-specific differential gene expression profiles (Supplementary Table 3) by comparing for each gene the expression by cells within each cluster to the expression by all cells outside the cluster using Wilcoxon rank-sum test. We then used cluster-specific gene expression patterns to infer the type of cells represented by each cluster.

Using these methods, we identified 8 clusters as different types of stromal cells typical of brain tissue, including astrocytes, oligodendrocytes, macrophages/microglia, vascular cells, fibroblasts and ciliated cells resembling ependymal or choroid plexus cells (Table 1; Fig. 2b). These 8 clusters localized as discrete single-cluster units on the UMAP projection. The other 14 clusters localized to a multi-cluster complex in which each cluster shared a border with other clusters. We identified these 14 clusters as tumor cells in a range of states that paralleled CGNP development, from proliferative cells at different phases of the cell cycle to non-proliferative cells at different stages of neural differentiation (Table 1). We identified proliferative clusters by expression of proliferation marker *Mki67*, Cyclin expression and SHH transcription factor *Gli1*, and further characterized proliferative cells as quiescent, cycling or M-phase enriched based on cluster-specific gene expression (Table 1). The non-proliferative clusters showed successive expression of early to later differentiation markers *Barhl1*, *Cntn2*, *Rbfox3* and *Grin2b* (Table 1; Fig 2c), as in our prior study of *M-Smo* tumors (10). We included CGNs as the most differentiated cell type within this group.

Cluster	Cell type designation	distinctive markers
0	early differentiating CGNP-like tumor cells	Pde1c, Nhlh1/2
1	proliferative, quiescent tumor cells	Hes1, Ccnd1
2	proliferative, quiescent tumor cells	Srebf1, Ccnd2
3	proliferative, quiescent tumor cells	Srebf1, Ccnd1
4	proliferative, cycling tumor cells	Top2a, Lig1, Esco2
5	differentiating CGNP-like tumor cells	Mtss1, Cntn2
6	proliferative, cycling tumor cells	Hells, rrm2
7	proliferative, cycling tumor cells, M phase enriched	Cdc20, Cenp1
8	proliferative, cycling tumor cells, M phase enriched	Aspm, Ccnb1
9	late differentiating CGN-like	Pcp4, Car10
10	differentiating CGN-like tumors	Cntn2, Nhlh1
11	proliferative, cycling tumor cells	Hells, Lig1, Pclaf
12	proliferative, cycling tumor cells	Hells, Lig1, Gli1
13	CGNs and CGN-differentiated tumor cells	Gabra6, Vsnl1
14	oligodendrocytes	Ptpz1, Sox10, Fabp7, Olig1/2
15	M2 microglia/macrophages	Mrc1, C1qb, Aif
16	astrocytes	Aldoc, Aqp4, Fabp7
17	fibroblasts	Lum, Vtn
18	endothelial cells	Cldn5, Flt1
19	M1 microglia/macrophages	Selplg, Siglech, C1qa, Aif
20	ependymal/choroid plexus cells	Rsph1, Folr1
21	myelinating oligodendrocytes	Opalin, Plp

Table 1. Identification of clusters as specific types of tumor and stromal cells

To compare the populations within *M-Smo* and *G-Smo* tumors, we deconvoluted the UMAP by genotype (Fig 2d). For quantitative comparison, we determined the number of cells from each replicate animal in each cluster, normalized to the total number of cells from that animal, and then compared the cluster populations from replicate *M-Smo* and *G-Smo* mice (Fig. 2d,e). We found that most tumor cell clusters were similarly populated in *M-Smo* and *G-Smo* tumors. However, Clusters 1, 2 and 7, within the proliferative region, were significantly enriched in *G-Smo* tumors ($p = 0.008$ for each by Wilcoxon rank-sum test), while cluster 13, comprising CGNs at the differentiated pole, was significantly enriched in the *M-Smo* tumors ($p = 0.023$).

Statistically significant enrichment of smaller magnitude was also seen in fibroblast ($p = 0.023$) and differentiated oligodendrocyte clusters ($p = 0.008$) in *M-Smo* tumors.

The similarity in the populations of most clusters in *G-Smo* and *M-Smo* tumors was consistent with the similarity of these tumors in bulk transcriptomic studies. The differential representation of specific types of tumor and stromal cells in *G-Smo* and *M-Smo* tumors, however demonstrated differences in tumor subpopulations that could not be detected using bulk transcriptomic analysis. *G-Smo* tumors showed increased proliferation, while *M-Smo* tumors showed increased differentiation, and were specifically depleted in the cell types represented by clusters 1,2 and 7. The expression patterns of all genes detected in our studies can be plotted and compared in *G-Smo* and *M-Smo* UMAPs through our web-based application: <https://gsmovmsmviewer.shinyapps.io/GvMviewer/>.

***G-Smo* tumors show larger populations of cells expressing stem cell markers**

To characterize further clusters 1, 2 and 7 that were composed predominantly of *G-Smo* cells, we defined the set of genes differentially up-regulated in these clusters compared to all tumor cells in *M-Smo* mice, excluding stromal cell types (Supplementary Table 4). We excluded stromal cells in order to prevent stromal gene expression patterns from obscuring differences in tumor cell gene expression. We noted that Clusters 1,2 and 7 showed increased expression of genes associated with stem cell phenotype, including *Nes*, *Vim*, *Olig1* and *Olig2*. Feature plots of each of these genes confirmed increased expression in *G-Smo* tumors, particularly in the region of Clusters 1,2 and 7 (Fig. 2f). We selected *Olig2* for further study, because recent functional genetic studies have shown that *Olig2*⁺ tumor cells in medulloblastoma are cancer stem cells that play an important role in medulloblastoma initiation and recurrence (24).

Different temporal patterns of stem cell behavior in *M-Smo* and *G-Smo* tumors

To confirm differential expression of *Olig2* at the protein level and to compare the temporal course of *Olig2* expression efficiently between genotypes, we labeled tumor sections using immunohistochemistry. Our scRNA-seq data showed that both oligodendrocytes and tumor stem cells express *Olig2*, and that oligodendrocytes can be distinguished from stem cells by the expression of *Sox10* (Fig. 2b,f). Labeling tumor sections with OLIG2 and SOX10 antibodies demonstrated both OLIG2⁺/SOX10⁺ cells that we considered to be oligodendrocytes and OLIG2⁺/SOX10⁻ cells that we considered to be OLIG2-expressing tumor stem cells, equivalent to the *Olig2*⁺ cells of clusters 1, 2 and 7. Prior studies found that OLIG2⁺ tumor stem cells were more numerous in the early stages of medulloblastoma tumorigenesis and decreased as tumors enlarged (18). To compare OLIG2 dynamics over time in *G-Smo* and *M-Smo* tumors, we analyzed sections of both genotypes at P5 and P15.

We found that at P5 both *M-Smo* and *G-Smo* comprised similarly large fractions of OLIG2⁺/SOX10⁻ cells (Fig 3b,c). The OLIG2⁺/SOX10⁻ fraction decreased over time in both genotypes, but the decrease was more marked in *M-Smo* tumors (Fig. 3d,e). Prior studies showed that sub-curative cytotoxic treatment of medulloblastoma with radiation or chemotherapy induces proliferation of stem cells in the perivascular niche, and that these cells express OLIG2 (24, 25). We compared the dynamics of the OLIG2⁺/SOX10⁻ population in *G-Smo* and *M-Smo* tumors recurring after treatment. We subjected P11 *G-Smo* and *M-Smo* mice to cytotoxic treatment with etoposide at a dose calibrated to produce regression followed by recurrence, and then we quantified OLIG2⁺/SOX10⁻ cells 4 days later, at P15. Compared to untreated tumors at P15, we noted increased expression of OLIG2 in SOX10⁻ cells, particularly in perivascular regions (Fig. 3f,g). Quantification of OLIG2⁺/SOX10⁻ cells in tumor sections showed that these populations were similar at P5, but significantly smaller in *M-Smo* tumors at P15, and that etoposide induced a significant increase in *M-Smo* tumors to levels similar to untreated P15 *G-Smo* tumors (Fig 3h). The OLIG2⁺/SOX10⁻ populations in *M-Smo* tumors were therefore not fixed, but rather were dynamic and varied inversely with tumor size, declining over time as tumors grew, and increasing after tumor shrinkage imposed by etoposide. The OLIG2⁺/SOX10⁻ fractions in *G-Smo* tumors, in contrast, showed a smaller decline over time and varied less across all conditions tested.

Similar range of cell fates in *G-Smo* and *M-Smo* tumors

We examined whether the differences in stem cell populations of *G-Smo* and *M-Smo* tumors were accompanied by an expansion of tumor cell fates. We previously found by lineage tracing using the 3' *Yfp* sequence of *SmoM2* that *SmoM2*-induced tumorigenesis in *M-Smo* mice expanded the typically neuronally-restricted *Atoh1* lineage to include astrocytic and oligodendrocytic progeny (10). Comparison of *Yfp* expression in *G-Smo* and *M-Smo* tumors showed that tumor lineage in both genotypes included neural progenitor-like tumor cells, differentiated neurons, astrocytes and oligodendrocytes (Fig. 4a). Cells within the fibroblast and macrophage/microglia clusters did not express *Yfp*, and while individual *Yfp*⁺ cells were noted in the endothelial and ependymal clusters, these rare cells did not indicate a significant trend as they were not observed in more than one replicate of either genotype. Glial cells were therefore the only stromal cell types that derived from the tumor lineage in either stem cell-derived or progenitor-derived tumors.

We compared the expression of specific neural markers to assess differences in tumor cell fates. In *G-Smo* tumors, the *Gfap-Cre* transgene is expected to activate *SmoM2* in a lineage that is broader than the *Atoh1* lineage activated by *Math1-Cre* in *M-Smo* tumors. The *Atoh1* lineage comprises rhombic-lip derived CGNP and unipolar brush cell populations, marked by *Barhl1* and *Eomes* (26) respectively. The set of neuronal cell types with *SmoM2* activation in *G-Smo* tumors includes these rhombic-lip derived populations, NESTIN⁺/ATOH1- EGL cells that also generate CGNs, and ventricular-zone derived GABAergic interneurons and progenitors, marked by expression of *Ascl1*, *Pax3* and *Pax2* (10).

To determine if *G-Smo* tumors contained more cells resembling ventricular zone-derived progenitors, we compared expression of *Barhl1*, *Eomes*, *Ascl1*, *Pax3* and *Pax2* in *G-Smo* and *M-Smo* tumors. We found that both genotypes consisted predominantly of *Barhl1*⁺ cells. We detected a significant genotype-specific difference within the *Atoh1* lineage, with a higher proportion of *Barhl1*⁺ cells in *G-Smo* tumors ($p < 1.0 \times 10^{-15}$, two-proportions z-test) and a higher proportion *Eomes*⁺ in *M-Smo* tumors ($p < 1.0 \times 10^{-15}$) (Fig. 4 b-c). However, we did not detect statistically significant differences in the populations of *Ascl1*, *Pax3* and *Pax2* expressing cells that define the lineage of GABA-ergic interneurons derive from the ventricular zone (Fig. 4d). Although *Gfap-Cre* activated *SmoM2* in both the rhombic lip and ventricular zone lineages, cells showing ventricular zone lineage were not expanded in *G-Smo* tumors. Based on the similarity of cell types showing *Yfp* in *G-Smo* and *M-Smo* tumors, and the similar, rare expression of ventricular zone markers, we conclude that differences between *G-Smo* and *M-Smo* tumors derive from effects of the timing of oncogenic event on cells that progress through the CGN developmental trajectory, rather than from the recruitment of interneuron lineage cells for tumor growth.

Different stromal populations in *M-Smo* and *G-Smo* tumors

To determine if *M-Smo* and *G-Smo* tumors may interact differently with stromal cells in their microenvironments, we compared gene expression in endothelial cell, myeloid cells and fibroblasts. We selected these cell types because they were the most numerous cell types outside the tumor lineage. To identify tumor-specific changes in these populations, and to distinguish tumor-specific effects common

to both tumor genotypes from effects specific to individual tumor genotypes, we combined the scRNA-seq data from *G-Smo* and *M-Smo* tumors with previously obtained data from WT cerebella at P7 (10). We obtained an initial grouping of cells from tumors and WT mice by cell type using the Harmony algorithm, which co-clustered tumor cells and their most similar normal progenitors (27). Using Harmony, we generated a UMAP combining *G-Smo*, *M-Smo* and WT cells, color-coded the clusters and analyzed cluster-specific gene expression profiles; of the proliferative cell types, CGNPs and medulloblastoma cells, grouped together in a set of *Barhl1+* clusters, while interneuron progenitors formed a separate group distinguished by *Pax3* and *Pax2* (Supplementary Fig. 1, Supplementary Table 5). We identified each stromal cell type based on gene expression (Fig. 5a, Supplementary Table 5), and isolated the endothelial, macrophage/microglial and fibroblastic populations. We then subjected the cells of each isolated cell type to a new PCA to sub-cluster each cell type.

Endothelial cells show cancer-specific changes without reflecting developmental differences between tumors

Endothelial cells showed significant differences between WT and tumor, but did not show statistically significant differences between *G-Smo* and *M-Smo* tumors. Unsupervised analysis defined 2 clusters (Fig. 5b). Cluster E0 was populated mostly by cells from WT cerebella with both tumor genotypes contributing similar fractions, while cluster E1 was populated predominantly by cells from the tumors, with no statistically significant difference in *G-Smo* and *M-Smo* contributions (Fig. 5c,d). Both clusters showed widespread expression of the endothelial markers *Pecam1* and *Cldn5*, confirming their endothelial cell identity (Fig. 5e). Each cluster showed cluster-specific gene expression (Fig. 5f,g, Supplementary Table 6). Cluster E1, which was predominantly populated by tumor-derived endothelial cells, showed increased expression of genes likely to contribute to malignancy, including the VEGF receptor *Flt1*, the p-Glycoprotein *Abcb1a* (aka *Mdr1*), and the CXCR4 ligand *Cxcl12* (aka *Sdf1*), which has been shown to promote medulloblastoma growth and glioblastoma-endothelial interactions (28-31). scRNA-seq thus detected biologically relevant differences between endothelial populations in WT cerebella and tumors, with tumor-specific effects that were shared between tumor genotypes, consistent with their overall similarity.

Developmental differences alter subsequent tumor-associated myeloid populations

The cells with myeloid characteristics, in contrast to endothelial cells, differed significantly between *M-Smo* and *G-Smo* tumors. Unsupervised analysis grouped the myeloid-like cells into 5 clusters, M0-M4 (Fig. 6a). Projection of *C1qb* expression confirmed that clusters M0-M3 were populated by myeloid cells (Fig. 6b). In contrast, cluster M4, which was the least populated, was *C1qb*- and expressed *Cnn3* and *Meis1* (Fig. 6b); this marker pattern identified cluster M4 as choroid plexus epithelial cells that have been noted to cluster with myeloid cells in other scRNA-seq analyses (32).

To identify the types myeloid cells, we defined the sets of genes up-regulated by cells within each cluster, compared to cells in the other 4 clusters (Supplementary Table 7), and then projected these genes on a UMAP along with other known markers of phenotype (Fig. 6c-f). Clusters M0 and M1, which localized to

clusters on one side of the UMAP, expressed *Cx3cr1* which distinguished them as microglia, while clusters M2 and M3, opposite in the UMAP, showed minimal *Cx3cr1*, indicating that they were macrophages (Fig. 6c). Cells of cluster M0 showed highly specific expression of *Sparc* (Fig. 6c), identifying these cells as mature, ramified microglia (33). Cluster M1 microglia specifically expressed *Mrc1*, *Igf1* and *Wfdc17* (Fig. 6d) which have all been linked to an M2-like, anti-inflammatory phenotype (34-36). Cluster M2 macrophages specifically expressed MHCII components, including Histocompatibility 2, Class II Antigen E alpha (*H2-Ea*) and the Invariant Polypeptide of Major Histocompatibility Complex, Class II Antigen-associated (*Cd74*) as well as *Il1b* and *Ccr2* (Fig. 6e), consistent with a pro-inflammatory M1-like phenotype (37-39). Importantly *Ccr2*+ macrophages have previously been shown to exert an anti-tumor effect in a medulloblastoma (39). Cluster M3 macrophages specifically expressed *Cd163* and *Mrc1* (Fig. 6f), also consistent with an anti-inflammatory M2 phenotype (40, 41). Myeloid cells thus resolved into microglial and macrophage populations, each with M1-like and M2-like subsets (Table 2).

Cluster	Cell type designation	distinctive markers
M0	Mature microglia	<i>Cx3cr1</i> , <i>Sparc</i>
M1	M2 microglia	<i>Igf1</i> , <i>Wfdc17</i> , <i>Mrc1</i>
M2	M1 macrophages	<i>Ccr2</i> , <i>Cd74</i> , <i>H2-Ea</i> , <i>Il1b</i>
M3	M2 macrophages	<i>Cd163</i> , <i>Mrc1</i>
M4	choroid plexus epithelial cells	<i>Cnn3</i> , <i>Meis1</i>

Table 2. Identification of clusters with myeloid characteristics (M0-M4)

Each cluster was differently populated by cells from *G-Smo*, *M-Smo* and WT cerebella (Fig 6g,h). The M1-like microglial clusters M0 and the non-myeloid cluster M4 comprised cells from all 3 genotypes. The M2-like microglial cluster M1 was tumor-specific and comprised cells from both *G-Smo* and *M-Smo* tumors. The M1-like macrophage cluster M2 predominantly comprised cells from *M-Smo* tumors. The M2-like macrophage cluster M3 comprised cells from *M-Smo* tumors and WT cerebella. These analyses showed that *M-Smo* tumors included M1-like and M2-like microglia (clusters M0 and M1), and M1-like and M2-like macrophages (cluster M2 and M3). In contrast the myeloid populations of *G-Smo* tumors were more limited, and the macrophage populations of cluster M2 and M3 were significantly smaller.

To confirm differential marker expression at the protein level, we visualized the protein expression of the MHCII glycoprotein coded by *H2-Ea* (H2-EA) and the pan macrophage/microglial marker IBA1 using immunohistochemistry (Fig. 6i). Consistent with the scRNA-seq data, comparison of H2-EA and IBA1 immunostaining in sections of each genotype showed that H2-EA+ macrophages were more prevalent in *M-Smo* tumors (Fig. 6j). These results confirm that protein expression patterns match transcript data from scRNA-seq and demonstrate that immunohistochemical staining for MHCII components was sufficient to distinguish between *G-Smo* and *M-Smo* tumors.

Differential cytokine expression in *G-Smo* and *M-Smo* tumors.

To consider potential mechanisms for the differences in macrophage populations in the two tumor types, we compared cytokine expression. To analyze a complete list of known cytokines and chemokines, we

used the set of 232 genes tagged with the Gene Ontology term “Cytokine Activity”. For each gene, we conducted differential expression testing between *G-Smo* and *M-Smo* tumors. Macrophage Migration Inhibitory Factor (*Mif*) was the only differentially expressed cytokine, and was higher in *G-Smo* tumors compared to *M-Smo* tumors (Fig. 6k). Intriguingly, *Mif* is a ligand for CD74 (42), and the *Cd74+* population was markedly lower in *G-Smo* tumors. Prior studies in melanoma have shown that intercellular communication through the MIF-CD74 interaction is immunosuppressive, and that blocking MIF-CD74 interaction increases tumor-associated M1 macrophages (43). Based on the inverse correlation of MIF and CD74 in our tumor model and on the prior studies of MIF-CD74 interaction in melanoma, we propose that MIF functions similarly in medulloblastoma to reduce the infiltration of CD74- expressing Cluster M2 macrophages, and acts more effectively in *G-Smo* tumors, which have higher *Mif* expression.

Developmental differences influence tumor fibroblast populations

The fibroblast populations in *G-Smo*, *M-Smo* and WT, similarly formed 3 clusters in unsupervised analysis, with significant differences between *G-Smo* and *M-Smo* tumors (Fig. 7a,b). Cluster F0 was WT-specific, Cluster F1 was WT and *M-Smo*-specific, and Cluster F2 was tumor-specific and populated with cells from both *G-Smo* and *M-Smo* tumors (Fig. 7b,c). Each cluster demonstrated different sets of cluster-specific gene expression patterns (Fig. 7d-f, Supplementary Table 8). We noted genotype specific effects on genes related to retinoid signaling, with *Fabp5* expressed predominantly in WT fibroblasts and *Rbp4* and *Crabp2* expressed by fibroblasts from both WT cerebella and *M-Smo* tumors, but not by fibroblasts from *G-Smo* tumors (Fig. 7g). These differential patterns show that non-cell autonomous effects of the timing of oncogenesis occur in fibroblastic stroma as well as in tumor-associated myeloid cells.

Discussion

Our data show that medulloblastomas initiated by a common driver mutation at different points in a developmental trajectory can show similar transcriptomic profiles but contain different populations of tumor and stromal cells and respond differently to therapy. *G-Smo* and *M-Smo* tumors both showed transcriptomic profiles in microarray studies that were consistent with SHH- subgroup medulloblastoma. However, scRNA-seq analysis demonstrated that *G-Smo* tumors, generated by initiating *SmoM2* expression in *Gfap*-expressing CNS stem cells, contained more proliferating cells at P15 and more *Olig2+* tumor stem cells. In contrast, *M-Smo* tumors, generated by initiating *SmoM2* expression in *Atoh1*-expressing committed neural progenitors, contained more differentiating tumor cells at P15, and more diverse macrophage/microglial and fibroblastic stroma. Differences in developmental history, therefore did not produce large differences in global gene expression profile, but significantly altered the heterogeneity within tumors, producing differences in the gene expression patterns of subsets of cells.

Analysis of *Olig2+* stem cell populations across time showed that the temporal pattern of stem cell regulation was different in *M-Smo* and *G-Smo* tumors. In the early stages of tumor growth at P5, both *G-Smo* and *M-Smo* tumors consisted mostly of OLIG2+ stem cells. As tumors grew over time, the fraction of OLIG2+ cells decreased in both genotypes, but *G-Smo* tumors retained larger OLIG2+ stem cell

populations. The difference in the timing of oncogene activation was thus sufficient to alter stem cell regulation in tumor cells many generations later, weeks after tumor initiation.

In addition to the differences within the tumor lineage, *G-Smo* and *M-Smo* tumors also showed significant differences in specific types of stromal cells. Not all stromal cell types showed strong differences between *G-Smo* and *M-Smo* tumors. Endothelial cells from tumors were significantly different from endothelial cells from WT cerebella, with a marked increase in the expression of the ABCB1 (aka MDR1) drug efflux pump. However, these tumor-specific patterns of gene expression were seen in endothelial cells from both *G-Smo* and *M-Smo* tumors. In contrast, myeloid and fibroblastic cells showed differences both between tumor versus WT and *G-Smo* versus *M-Smo* tumors, with *M-Smo* tumors having a more diverse stromal cell composition. Different patterns of cytokine expression, with increased *Mif* expression in *G-Smo* tumors, may mediate these differences. These differences show that the timing of oncogenesis can affect tumor composition both by altering the heterogeneity of tumor cells and by altering the ways that tumor cells interact with cells of the tumor microenvironment.

The developmental differences between *G-Smo* and *M-Smo* tumors are complex and include differences in both timing and lineage. *Gfap* expression, and thus *SmoM2* activation in *G-Smo* tumors, begins earlier than *Atoh1* expression and *SmoM2* activation in *M-Smo* tumors. Moreover, the *Gfap-Cre* transgene is likely to activate *SmoM2* in *Nes+ / Atoh1-* neural stem cells in the EGL; these cells are known to be SHH sensitive but do not express *Atoh1* and thus are likely not to be targeted by *Math1-Cre*. As a result, *G-Smo* tumors initiate in both *Atoh1+* and *Nes+ / Atoh1-* lineages, while *M-Smo* tumors initiate in only the *Atoh1+* lineage. However, we have previously shown that *SmoM2* activation relaxes lineage restriction in *M-Smo* tumors, increasing the tendency of *Atoh1*-lineage cells to take on glial fates (10). The lineage and timing differences are thus interlinked and may be impossible to deconvolute. The net result, however, is to produce consistent differences in tumor heterogeneity.

Both *Olig2*-expressing tumor stem cells and *Ccr2*-expressing macrophages have been shown to affect tumor progression and prognosis (24, 39), and each may contribute to the differences we noted in survival and treatment. Prior studies show that targeting the *Olig2*+ population, either by conditional ablation of *Olig2*-expressing cells using HSV TK or conditional genetic deletion of the *Olig2* locus has been shown to reduce the growth of SHH-driven medulloblastomas in mice, extending animal survival (24). Similarly, ablation of *Ccr2*-expressing macrophages has been shown to shorten the survival of mice with SHH-driven medulloblastoma, indicating that this specific macrophage population exerts an important anti-tumor effect (39). *G-Smo* tumors showed both increased *Olig2*+ stem cells and decreased *Ccr2*+ macrophages, demonstrating two mechanisms that are each sufficient to worsen prognosis.

Our data show that developmental events that would be cryptic in a clinical setting can influence clinical outcome by affecting both tumor cells and stroma. While these effects passed undetected in histologic analysis and bulk transcriptomic studies, counting OLIG2+ tumor cells or MHCII-expressing macrophages provided effective biomarkers that distinguished radioresistant stem cell-derived tumors from radiosensitive tumors originating in CGNPs. These biomarkers succeeded because they were sensitive to

differences in cellular heterogeneity. Effective prognostication and precision therapy require supplementing transcriptomic analysis with biomarkers that can detect differences in important sub-populations within tumors.

Tumor heterogeneity, *Olig2*⁺ populations and myeloid subtypes are all readily measurable. While scRNA-seq identified differences between tumors, each of these differences can be probed in clinical samples using IHC or flow cytometry, which preserve cellular information that is lost in transcriptomic analysis. Future studies are needed to determine whether analysis of these parameters provides prognostic information that reduces the heterogeneity of transcriptomic subgroups.

Methods

Mice

We crossed *SmoM2* mice (Jackson Labs, stock # 005130) with *GFAP-Cre* mice (Jackson Labs, stock # 004600), to generate *G-Smo* mice, and with *Math1-Cre* (Jackson Labs, stock #011104) to generate *M-Smo* mice. All mice were of species *Mus musculus* and crossed into the C57BL/6 background through at least five generations. All animal studies were carried out with the approval of the University of North Carolina Institutional Animal Care and Use Committee under protocols (19-098).

Histology and immunohistochemistry

Mouse brains were processed, immunostained and quantitatively analyzed as previously described (10, 20, 44). Primary antibodies used were: OLIG2 diluted 1:100 (Cell Marque, # 387R-14), SOX10 diluted 1:200 (Cell Signaling Technology, #7833S), MHC Class II glycoprotein H2-EA, diluted 1:200 (Novus, # NBP1-43312), IBA1 1:2000 (Wako Chemicals, #019-19741).

Stained images were counterstained with DAPI, digitally imaged using an Aperio Scan Scope XT (Aperio) and subjected to automated cell counting using Tissue Studio (Definiens).

Radiation therapy and survival studies

Medulloblastoma-bearing mice were treated with 10Gy x-ray irradiation, delivered as 5 fractions of 2Gy each, as previously described (20). Briefly, starting P10, *G-Smo* and *M-Smo* mice were irradiated daily for 5 days. Irradiation was performed under general anesthesia with isoflurane, delivered by vaporizer through nose cones, after which mice were allowed to recover and then returned to their dams. Following radiation therapy, radiation-treated mice and untreated littermate controls were observed for symptoms of tumor progression, including movement disorder, ataxia or sustained weight loss. Mice showing symptoms of progression were euthanized, and the time to progression was considered to be the EFS. Brain pathology was analyzed to confirm tumor progression.

Microarray analysis

Medulloblastomas were harvested from P15 *G-Smo* and *M-Smo* mice and immediately flash frozen. Frozen tissue was homogenized by sonication in RLT buffer (Qiagen), and total RNA was purified following manufacturer's instructions (QIAGEN, cat#74104). RNA was labeled, hybridized to Affymetrix Mouse Gene 2.1ST arrays, per manufacturer's protocol (Affymetrix, Santa Clara, CA USA) and scanned by the UNC-Lineberger Genomics core. Microarray analysis was performed using the Partek Genomics Suite (Partek Incorporated, St. Louis, Missouri). 1- way ANOVA was used to identify genes that varied significantly between the two genotypes.

Tissue Preparation for Drop-seq

Mice were anesthetized using isoflurane and then euthanized via decapitation. The brain was divided along the sagittal midline and one half was processed for histology while a large sample of tumor was dissected from the other half and processed for Drop-seq analysis. This sample was dissociated using the Papain Dissociation System (Worthington Biochemical) following the protocol used in previous studies (10, 45). Briefly, tumor samples were incubated in papain at 37 °C for 15 min, then triturated and the suspended cells were spun through a density gradient of ovomucoid inhibitor.

Pelleted cells were then resuspended in 1 mL HBSS with 6 g/L glucose and diluted in PBS-BSA solution to a concentration of 95-110 cells/ μ L. Barcoded Seq B Drop-seq beads (ChemGenes) were diluted in Drop-seq lysis buffer to a concentration between 95-110 beads/ μ L. Tumor cells were co-encapsulated with barcoded beads using FlowJEM brand PDMS devices as previously described (10). All cells were processed within one hour of tissue dissociation. Droplet breakage and library preparation steps followed Drop-seq protocol V3.1 (46). After PCR, amplified cDNA was subjected Ampure XP cleanup at 0.6x and 1x ratios to eliminate residual PCR primers and debris. found by the bioanalyzer electropherogram. 1. If PCR failed to generate adequate cDNA, the PCR was repeated with the 3rd round increased from 11 to 13 cycles.

For QC purposes, library pools consisting of the tagmented cDNA from 2,000 beads/run were prepared and sequenced to low depth (~2.5M reads/2K beads). We used the resulting data to assess library efficiency, including total read losses to PolyA regions, nonsense barcodes and adapter sequences as well as the quality and number of the transcriptomes captured. Passable runs contained 40-60% of reads associated with the top 80-100 barcodes found in 2,000 beads. Drop-seq runs passing QC were then prepared for high-depth sequencing on an Illumina Hi-Seq 4000. Each sample underwent a new generation of bulk cDNA from the stored beads and was prepared with the same ratios as described above. Pools were formulated according to the number of cells/sample to avoid oversampling of each sample and to balance the reads per lane across the Hi-Seq.

Processing of scRNA-seq data

Full data analysis code is available at https://github.com/malawsky/Gershon_single-cell

Data analysis was performed using the Seurat R package version 3.1.1 (47). Data were subjected to several filtering steps. First, only genes that were detected in at least 30 cells were considered, to prevent misaligned reads appearing as rare transcripts in the data. Cells were then filtered using specific QC criteria to limit the analysis to cells with transcriptomes that were well-characterized and not apoptotic.

We noted that *G-Smo* cells were sequenced at a greater depth than *M-Smo* cells which can introduce unwanted batch effects into the analysis. Consistent with best practices (23), we downsampled the *G-Smo* cells to 60% of their original depth so as to achieve similar sequencing depth between *G-Smo* and *M-Smo* cells prior to further filtering.

Putative cells with fewer than 500 detected RNA molecules (nCount) or 200 different genes (nFeature) were considered to have too little information to be useful, and potentially to contain mostly ambient mRNA reads. Putative cells with greater than 4 standard deviations above the median nCount or nFeature were suspected to be doublets, improperly merged barcodes, or sequencing artifacts and were excluded. As in our previously published work, putative cells with more than 10% mitochondrial transcripts were suspected to be dying cells and also excluded (10).

In total, 53% of putative cells from *G-Smo* mice and 49% of putative cells from *M-Smo* mice met QC criteria and were included in the analysis. From the 6 *G-Smo* mice, we included a total of 8699 cells with a range of 802–2056 cells per animal and a median of 1481 cells. From the five *M-Smo* mice, we included a total of 5930 cells, with a range of 614–2512 cells per animal and a median of 821 cells.

scRNA-seq Data normalization, clustering, differential gene expression, and visualization The data was normalized using the SCTransform method as implemented in Seurat. The function then selected the top 3,000 most highly variable genes. PCA was performed on the subset of highly variable genes using the RunPCA function. The number of PCs to be used in downstream analysis was chosen to be 17 based on examining the elbow in the elbow plot as implemented by Seurat.

We used the FindNeighbors and FindClusters functions to identify cell clusters in the data. Briefly, these functions define a graph connecting cells to each other by weighted edges and then identify clusters in the graph that place each cell into a single cluster using the Louvain algorithm. For the FindClusters function, we found that a resolution of 1.2 produced biologically meaningful clusters.

To identify differential genes between clusters of cells, Wilcoxon rank sum test was used to compare gene expression of cells within the cluster of interest to all cells outside that cluster as implemented by the FindMarkers function. Specific parameters for the genes to be analyzed based on their log fold change between the two compared groups and percent of cells expressing the gene in at least one of the groups are available in the data analysis code. Uniform Manifold Approximation and Projection was used to reduce the PCs to two dimensions for data visualization using the RunUMAP function. For re-iterated analysis of the isolated stromal clusters, the same procedures were used with parameters changed as described in the data analysis code.

Cell-type identification

Following PCA and UMAP, we inspected clusters for expression of indicated markers using the differential gene expression results. Marker genes were plotted using an expression cutoff to facilitate the visualization of both high- and low-expression genes on a single plot. Cutoffs are applied so that only cells with expression >cutoff received the color corresponding to that gene. These cutoffs are available in the data analysis code. In feature plots of multiple genes, for individual cells expressing multiple markers, each gene was over-plotted in the order described in the code. Feature plots of genes will be made available upon reasonable request.

Harmony analysis

To merge the previously published WT dataset with the tumor dataset, we used the Harmony algorithm (27). First, the WT and tumor dataset were analyzed in single SCTransform normalization and PCA steps. The Harmony algorithm then used the cells' PCA coordinates and dataset identity to calculate new coordinates for each cell so as to minimize dataset dependence when applying clustering to the cells. This algorithm produced a dimensional reduction that was used in place of PCA with the same steps applied to the data as described in the "Data normalization, clustering, differential gene expression, and visualization" and "Cell-type identification" sections of the Methods.

Declarations

Data Availability

The microarray data was deposited Gene Expression Omnibus database and the accession code is pending. The scRNA-seq data were deposited in the Gene Expression Omnibus database under the accession code GSE150579. Expression data is also available through our web-based application: <https://gsmovmsmviewer.shinyapps.io/GvMviewer/>.

Acknowledgements

We thank Dr. David Rowitch and Dr. Robert Wechsler-Reya for sharing their invaluable editorial and scientific insight during the writing process. We thank the UNC CGBID Histology Core, supported by P30 DK 034987 and the UNC Tissue Pathology Laboratory Core supported by NCI CA016086. J.O. was supported by NINDS (F31NS100489). T.R.G. was supported by NINDS (R01NS088219, R01NS102627, R01NS106227) and by the UNC Department of Neurology Research Fund. T.R.G., K.W., and B.B. were supported by a TTSA grant from the NCTRACS Institute, which is supported by the National Center for Advancing Translational Sciences (NCATS), National Institutes of Health, through Grant Award Number UL1TR002489.

Author Contributions

D.M., S.J.W. and T.R.G. wrote the manuscript. D.M., S.J.W., J.O., and B.B. conducted the experiments and analyzed the data. K.W. and T.R.G. were responsible for conception and oversight of the project. All authors discussed the results and reviewed the manuscript.

Competing Interests

The authors declare no competing interests.

References

1. Northcott PA, Korshunov A, Witt H, Hielscher T, Eberhart CG, Mack S, et al. Medulloblastoma comprises four distinct molecular variants. *J Clin Oncol*. 2011;29(11):1408-14.
2. Cavalli FMG, Remke M, Rampasek L, Peacock J, Shih DJH, Luu B, et al. Intertumoral Heterogeneity within Medulloblastoma Subgroups. *Cancer Cell*. 2017;31(6):737-54
3. Zurawel RH, Allen C, Wechsler-Reya R, Scott MP, Raffel C. Evidence that haploinsufficiency of Ptch leads to medulloblastoma in mice. *Genes Chromosomes Cancer*. 2000;28(1):77-81.
4. Oliver TG, Read TA, Kessler JD, Mehmeti A, Wells JF, Huynh TTT, et al. Loss of patched and disruption of granule cell development in a pre-neoplastic stage of medulloblastoma. *Development*. 2005;132(10):2425-39.
5. Wechsler-Reya RJ, Scott Control of Neuronal Precursor Proliferation in the Cerebellum by Sonic Hedgehog. *Neuron*. 1999;22(1):103-14.
6. Dahmane N, Ruiz-i-Altaba A. Sonic hedgehog regulates the growth and patterning of the cerebellum. *Development*. 1999;126(14):3089-100.
7. Roussel MF, Hatten ME. Cerebellum development and medulloblastoma. *Curr Top Dev* 2011;94:235-82.

8. Hallahan AR, Pritchard JI, Hansen S, Benson M, Stoeck J, Hatton BA, et al. The SmoA1 mouse model reveals that notch signaling is critical for the growth and survival of sonic hedgehog-induced medulloblastomas. *Cancer Research*. 2004;64(21):7794-800.
9. Li P, Du F, Yuelling LW, Lin T, Muradimova RE, Tricarico R, et al. A population of Nestin- expressing progenitors in the cerebellum exhibits increased tumorigenicity. *Nat Neurosci*. 2013;16(12):1737-44.
10. Ocasio J, Babcock B, Malawsky D, Weir SJ, Loo L, Simon JM, et al. scRNA-seq in medulloblastoma shows cellular heterogeneity and lineage expansion support resistance to SHH inhibitor therapy. *Nat Commun*. 2019;10(1):5829.
11. Selvadurai HJ, Luis E, Desai K, Lan X, Vladioiu MC, Whitley O, et al. Medulloblastoma Arises from the Persistence of a Rare and Transient Sox2(+) Granule Neuron Precursor. *Cell Rep*. 2020;31(2):107511.
12. Zhuo L, Theis M, Alvarez-Maya I, Brenner M, Willecke K, Messing A. hGFAP-cre transgenic mice for manipulation of glial and neuronal function in vivo. *Genesis*. 2001;31(2):85-94.
13. Kuang Y, Liu Q, Shu X, Zhang C, Huang N, Li J, et al. Dicer1 and MiR-9 are required for proper Notch1 signaling and the Bergmann glial phenotype in the developing mouse cerebellum. *Glia*. 2012;60(11):1734-46.
14. Helms AW, Abney AL, Ben-Arie N, Zoghbi HY, Johnson JE. Autoregulation and multiple enhancers control Math1 expression in the developing nervous system. *Development*. 2000;127(6):1185-96.
15. Machold R, Fishell G. Math1 Is Expressed in Temporally Discrete Pools of Cerebellar Rhombic- Lip Neural Progenitors. *Neuron*. 2005;48(1):17-24.
16. Matei V, Pauley S, Kaing S, Rowitch D, Beisel KW, Morris K, et al. Smaller inner ear sensory epithelia in Neurog1 null mice are related to earlier hair cell cycle exit. *Developmental Dynamics*. 2005;234(3):633-50.
17. Yang Z-J, Ellis T, Markant SL, Read T-A, Kessler JD, Bourbonoulas M, et al. Medulloblastoma Can Be Initiated by Deletion of Patched in Lineage-Restricted Progenitors or Stem Cells. *Cancer Cell*. 2008;14(2):135-45.
18. Schüller U, Heine VM, Mao J, Kho AT, Dillon AK, Han Y-G, et al. Acquisition of Granule Neuron Precursor Identity Is a Critical Determinant of Progenitor Cell Competence to Form Shh-Induced Medulloblastoma. *Cancer Cell*. 2008;14(2):123-34.
19. Chow KH, Shin DM, Jenkins MH, Miller EE, Shih DJ, Choi S, et al. Epigenetic states of cells of origin and tumor evolution drive tumor-initiating cell phenotype and tumor Cancer Res. 2014;74(17):4864-74.
20. Crowther AJ, Ocasio JK, Fang F, Meidinger J, Wu J, Deal AM, et al. Radiation Sensitivity in a Preclinical Mouse Model of Medulloblastoma Relies on the Function of the Intrinsic Apoptotic Pathway. *Cancer Res*. 2016;76(11):3211-23.
21. Loo LZ, M. Drop seq brain. *Nat Commun*.
22. Vladioiu MC, El-Hamamy I, Donovan LK, Farooq H, Holgado BL, Ramaswamy V, et al. Childhood cerebellar tumors mirror conserved fetal transcriptional programs. *bioRxiv*. 2018:350280.

23. Luecken MD, Theis FJ. Current best practices in single-cell RNA-seq analysis: a tutorial. *Mol Syst Biol.* 2019;15(6):e8746.
24. Zhang L, He X, Liu X, Zhang F, Huang LF, Potter AS, et al. Single-Cell Transcriptomics in Medulloblastoma Reveals Tumor-Initiating Progenitors and Oncogenic Cascades during Tumorigenesis and Relapse. *Cancer Cell.* 2019;36(3):302-18
25. Hambardzumyan D, Becher OJ, Rosenblum MK, Pandolfi PP, Manova-Todorova K, Holland PI3K pathway regulates survival of cancer stem cells residing in the perivascular niche following radiation in medulloblastoma in vivo. *Genes & Development.* 2008;22(4):436-48.
26. Englund C, Kowalczyk T, Daza RA, Dagan A, Lau C, Rose MF, et al. Unipolar brush cells of the cerebellum are produced in the rhombic lip and migrate through developing white matter. *J Neurosci.* 2006;26(36):9184-95.
27. Korsunsky I, Millard N, Fan J, Slowikowski K, Zhang F, Wei K, et al. Fast, sensitive and accurate integration of single-cell data with Harmony. *Nat Methods.* 2019;16(12):1289-96.
28. Sengupta R, Dubuc A, Ward S, Yang L, Northcott P, Woerner BM, et al. CXCR4 activation defines a new subgroup of Sonic hedgehog-driven medulloblastoma. *Cancer Res.* 2012;72(1):122-32.
29. Rao S, Sengupta R, Choe EJ, Woerner BM, Jackson E, Sun T, et al. CXCL12 mediates trophic interactions between endothelial and tumor cells in glioblastoma. *PLoS One.* 2012;7(3):e33005.
30. Rubin JB, Kung AL, Klein RS, Chan JA, Sun Y, Schmidt K, et al. A small-molecule antagonist of CXCR4 inhibits intracranial growth of primary brain tumors. *Proc Natl Acad Sci U S A.* 2003;100(23):13513-8.
31. Klein RS, Rubin JB, Gibson HD, DeHaan EN, Alvarez-Hernandez X, Segal RA, et al. SDF-1 alpha induces chemotaxis and enhances Sonic hedgehog-induced proliferation of cerebellar granule cells. *Development.* 2001;128(11):1971-81.
32. Li Q, Cheng Z, Zhou L, Darmanis S, Neff NF, Okamoto J, et al. Developmental Heterogeneity of Microglia and Brain Myeloid Cells Revealed by Deep Single-Cell RNA Sequencing. *Neuron.* 2019;101(2):207-23
33. Lloyd-Burton SM, York EM, Anwar MA, Vincent AJ, Roskams AJ. SPARC regulates microgliosis and functional recovery following cortical ischemia. *J Neurosci.* 2013;33(10):4468-81.
34. Laoui D, Movahedi K, Van Overmeire E, Van den Bossche J, Schouppe E, Mommer C, et al. Tumor-associated macrophages in breast cancer: distinct subsets, distinct functions. *Int J Dev Biol.* 2011;55(7-9):861-7.
35. Spadaro O, Camell CD, Bosurgi L, Nguyen KY, Youm YH, Rothlin CV, et al. IGF1 Shapes Macrophage Activation in Response to Immunometabolic Cell Rep. 2017;19(2):225-34.
36. Karlstetter M, Walczak Y, Weigelt K, Ebert S, Van den Brulle J, Schwer H, et al. The novel activated microglia/macrophage WAP domain protein, AMWAP, acts as a counter-regulator of proinflammatory response. *J Immunol.* 2010;185(6):3379-90.
37. Diez M, Abdelmagid N, Harnesk K, Strom M, Lidman O, Swanberg M, et al. Identification of gene regions regulating inflammatory microglial response in the rat CNS after nerve injury. *J Neuroimmunol.* 2009;212(1-2):82-92.

38. Gensel JC, Zhang B. Macrophage activation and its role in repair and pathology after spinal cord injury. *Brain Res.* 2015;1619:1-11.
39. Maximov V, Chen Z, Wei Y, Robinson MH, Herting CJ, Shanmugam NS, et al. Tumour-associated macrophages exhibit anti-tumoural properties in Sonic Hedgehog medulloblastoma. *Nat Commun.* 2019;10(1):2410.
40. Jayasingam SD, Citartan M, Thang TH, Mat Zin AA, Ang KC, Ch'ng ES. Evaluating the Polarization of Tumor-Associated Macrophages Into M1 and M2 Phenotypes in Human Cancer Tissue: Technicalities and Challenges in Routine Clinical Practice. *Front Oncol.* 2019;9:1512.
41. Vogel DY, Glim JE, Stavenuiter AW, Breur M, Heijnen P, Amor S, et al. Human macrophage polarization in vitro: maturation and activation methods compared. *Immunobiology.* 2014;219(9):695- 703.
42. Leng L, Metz CN, Fang Y, Xu J, Donnelly S, Baugh J, et al. MIF signal transduction initiated by binding to CD74. *J Exp Med.* 2003;197(11):1467-76.
43. Figueiredo CR, Azevedo RA, Mousdell S, Resende-Lara PT, Ireland L, Santos A, et al. Blockade of MIF-CD74 Signalling on Macrophages and Dendritic Cells Restores the Antitumour Immune Response Against Metastatic Melanoma. *Front Immunol.* 2018;9:1132.
44. Ocasio JK, Bates RDP, Rapp CD, Gershon TR. GSK-3 modulates SHH-driven proliferation in postnatal cerebellar neurogenesis and medulloblastoma. *Development.* 2019;146(20).
45. Lang PY, Nanjangud GJ, Sokolsky-Papkov M, Shaw C, Hwang D, Parker JS, et al. ATR maintains chromosomal integrity during postnatal cerebellar neurogenesis and is required for medulloblastoma formation. *Development.* 2016;143(21):4038-52.
46. Macosko EZ, Basu A, Satija R, Nemesh J, Shekhar K, Goldman M, et al. Highly Parallel Genome-wide Expression Profiling of Individual Cells Using Nanoliter Droplets. *Cell.* 2015;161(5):1202-14.
47. Butler A, Hoffman P, Smibert P, Papalexi E, Satija R. Integrating single-cell transcriptomic data across different conditions, technologies, and species. *Nat Biotechnol.* 2018;36(5):411-20.

Figures

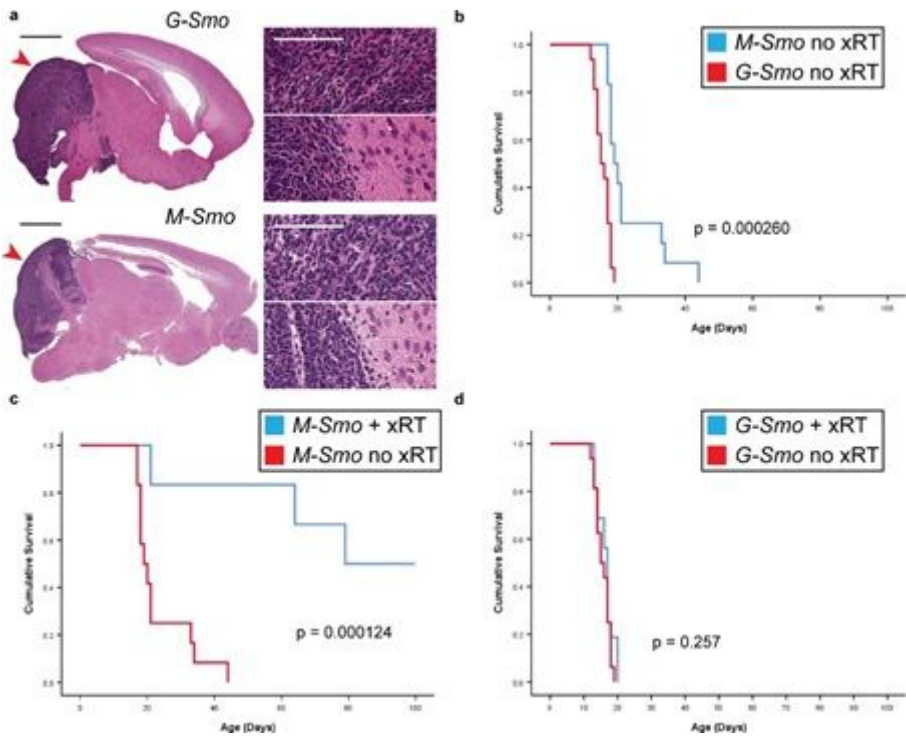


Figure 1

M-Smo and G-Smo tumors show similar histology but different rates of progression and responses to treatment. (A) Representative sagittal H&E-stained sections of each genotype at P15, with tumors highlighted by red arrowheads. Insets show regions within the tumors and regions at the tumor interface with adjacent brain. (B-D) Kaplan Meier curves comparing (B) survival of untreated mice of each genotype, (C) survival of M-Smo mice with and without xRT, and (D) survival of G-Smo mice with and without xRT. In (A) scale bars = 2 mm, or 100 μ m in insets.

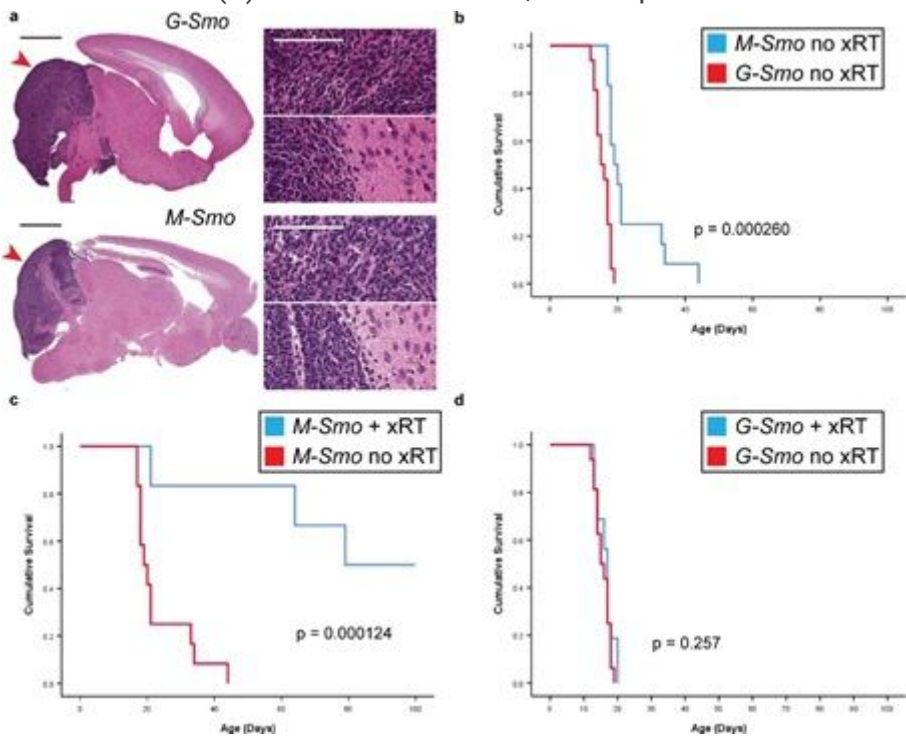


Figure 1

M-Smo and G-Smo tumors show similar histology but different rates of progression and responses to treatment. (A) Representative sagittal H&E-stained sections of each genotype at P15, with tumors highlighted by red arrowheads. Insets show regions within the tumors and regions at the tumor interface with adjacent brain. (B-D) Kaplan Meier curves comparing (B) survival of untreated mice of each genotype, (C) survival of M-Smo mice with and without xRT, and (D) survival of G-Smo mice with and without xRT. In (A) scale bars = 2 mm, or 100 μ m in insets.

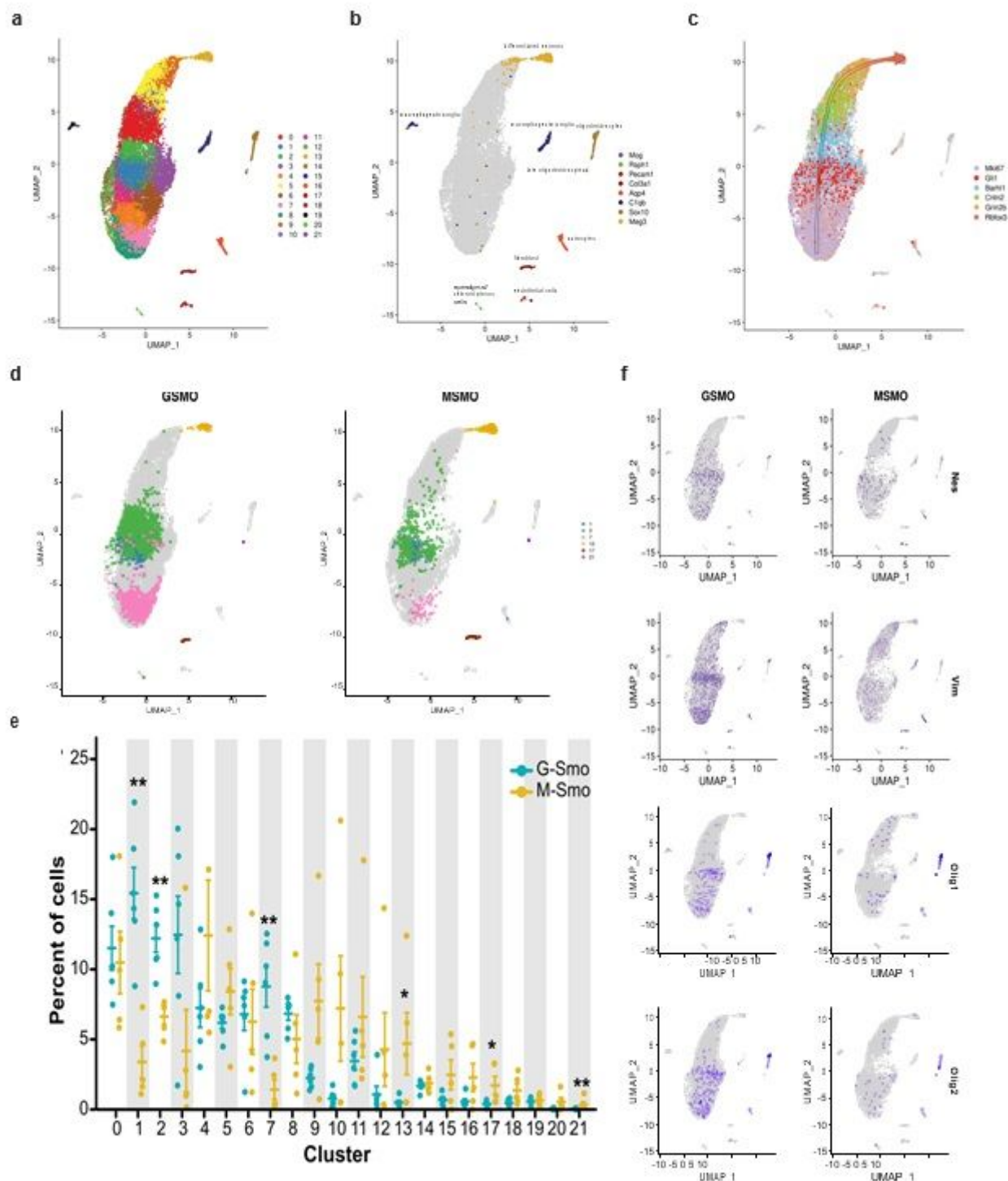


Figure 2

Similarities and differences in the subpopulations of G-Smo and M-Smo tumors. (A) UMAP plot of all cells from G-Smo and M-Smo tumors, color-coded by cluster. Cells are localized according to their proximity in PCA space. (B,C) Feature plots showing expression of (B) stromal markers, or (C) cerebellar granule neuron differentiation markers, color coded over the UMAP shown in (A) Arrow in (C) indicates the direction of differentiation across the UMAP. (D) UMAP plots deconvoluted by genotype, with differentially represented clusters color coded. (E) Comparison of each cluster population in G-Smo and M-Smo tumors. Dots represent values for individual replicates, bars indicate the means and whiskers indicate the SEM. ** indicates $p < 0.01$, * indicates $p < 0.05$. (F) UMAP plots for each genotype, showing expression of the indicated stem cell markers.

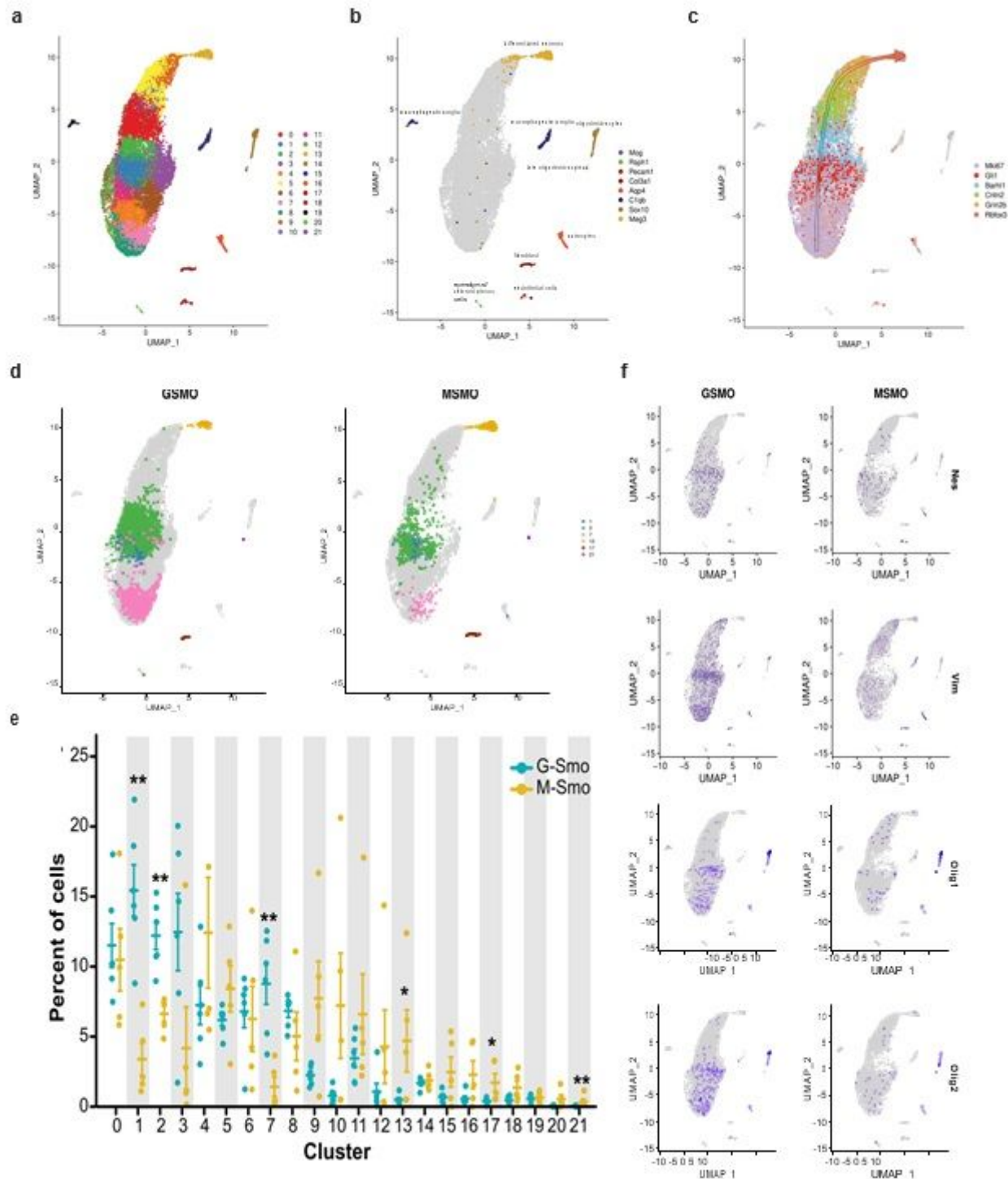


Figure 2

Similarities and differences in the subpopulations of G-Smo and M-Smo tumors. (A) UMAP plot of all cells from G-Smo and M-Smo tumors, color-coded by cluster. Cells are localized according to their proximity in PCA space. (B,C) Feature plots showing expression of (B) stromal markers, or (C) cerebellar granule neuron differentiation markers, color coded over the UMAP shown in (A) Arrow in (C) indicates the direction of differentiation across the UMAP. (D) UMAP plots deconvoluted by genotype, with differentially

represented clusters color coded. (E) Comparison of each cluster population in G-Smo and M-Smo tumors. Dots represent values for individual replicates, bars indicate the means and whiskers indicate the SEM. ** indicates $p < 0.01$, * indicates $p < 0.05$. (F) UMAP plots for each genotype, showing expression of the indicated stem cell markers.

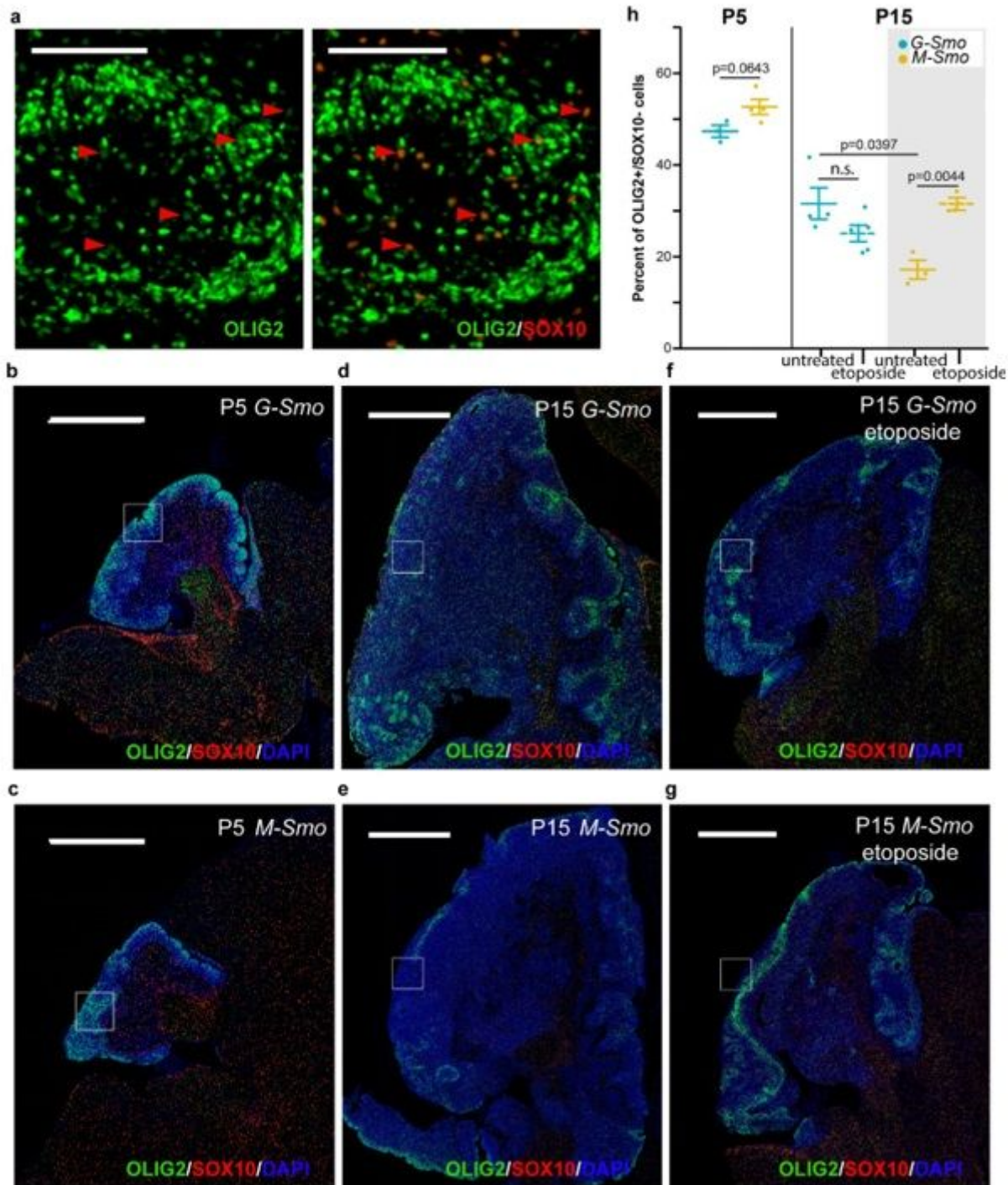


Figure 3

OLIG2+ stem cells decline more rapidly in M-Smo compared to G-Smo tumors. (A) Immunohistochemistry for OLIG2 (green) and SOX10 (red) in a representative section of a G-Smo tumor. Arrowhead show examples of OLIG2+ cells that also express SOX10. (B-G) Immunohistochemistry for OLIG2 (green and

SOX10 (red) in representative sagittal sections from mice of the indicated age and genotype. Scale bars = 100 μ m in (A) and 1 mm in (B-G) (H) Comparison of indicated populations in G-Smo and M-Smo tumors. Dots represent values for individual replicates, bars indicate the means and whiskers indicate the SEM.

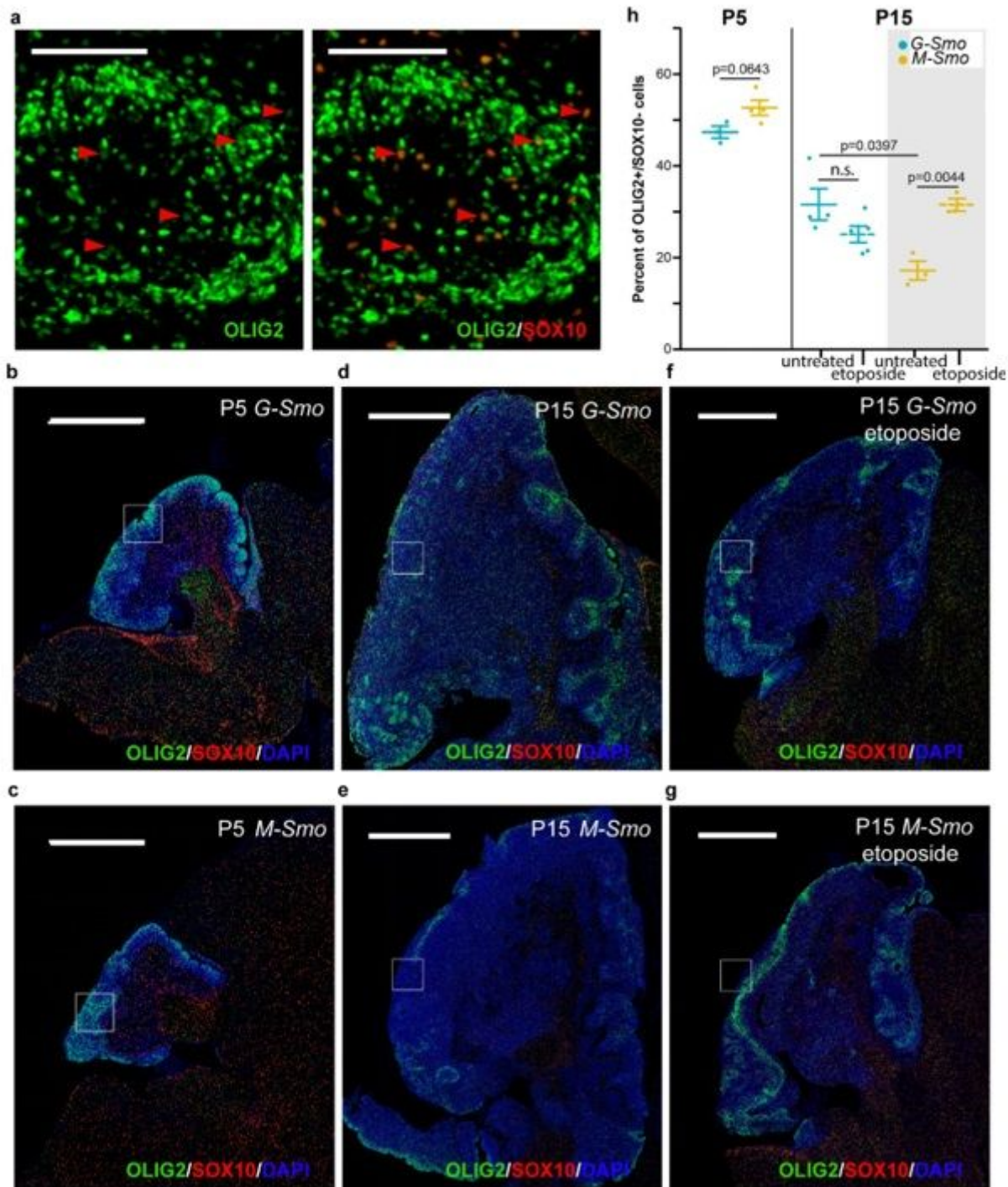


Figure 3

OLIG2+ stem cells decline more rapidly in M-Smo compared to G-Smo tumors. (A) Immunohistochemistry for OLIG2 (green) and SOX10 (red) in a representative section of a G-Smo tumor. Arrowhead show examples of OLIG2+ cells that also express SOX10. (B-G) Immunohistochemistry for OLIG2 (green and SOX10 (red) in representative sagittal sections from mice of the indicated age and genotype. Scale bars =

100 μ m in (A) and 1 mm in (B-G) (H) Comparison of indicated populations in G-Smo and M-Smo tumors. Dots represent values for individual replicates, bars indicate the means and whiskers indicate the SEM.

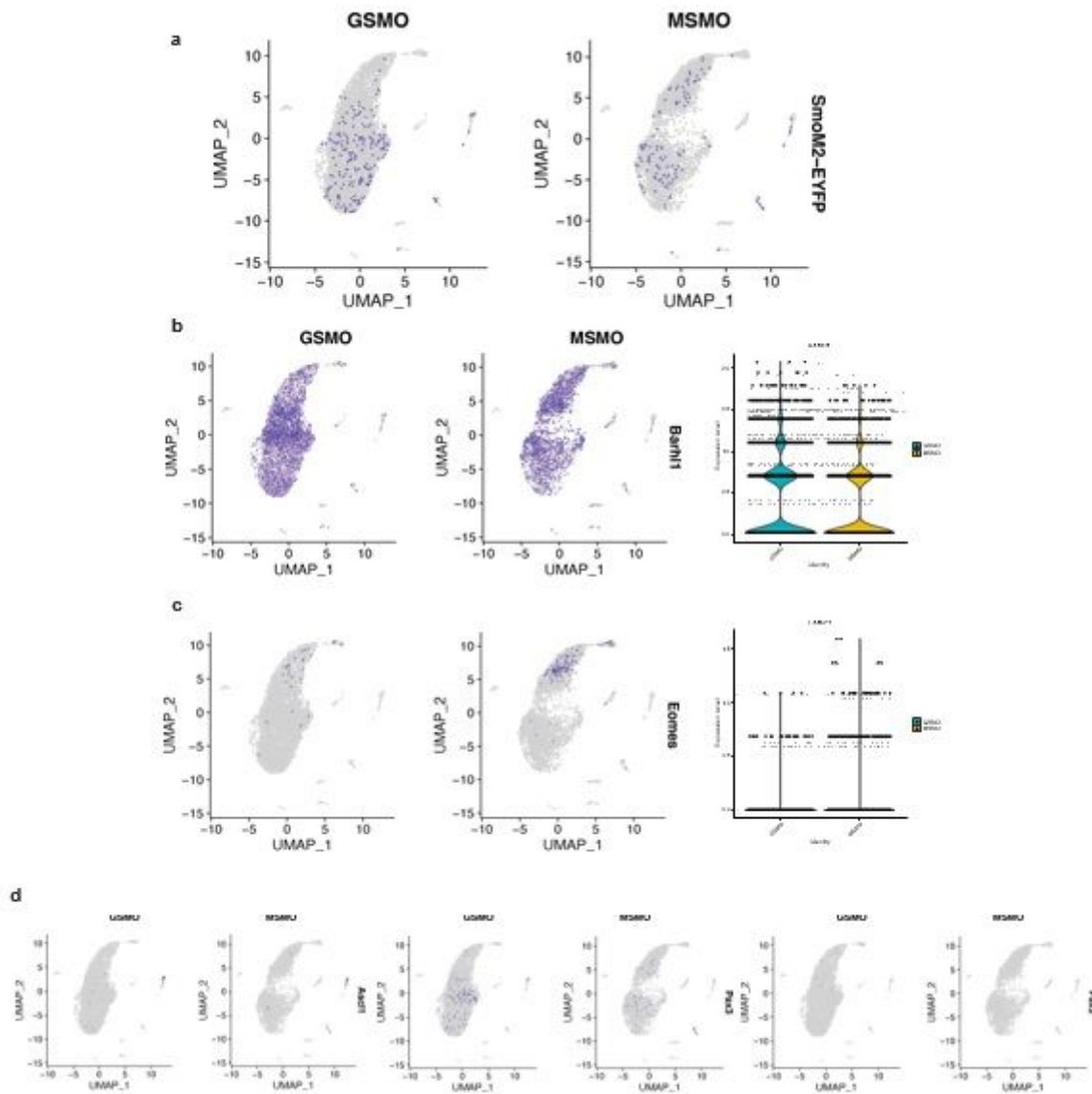


Figure 4

Similar range of cell fates in G-Smo and M-Smo tumors. Feature plots showing expression of the indicated lineage markers, color coded over the UMAP shown in (2D). (A) Yfp expression, denoting the SmoM2-activated lineage, was distributed similarly in both G-Smo and M-Smo tumors. Green circle shows oligodendrocytes; brown circle shows astrocytes. (B) G-Smo tumors showed increased Barhl1+ cells, consistent with a greater fraction of cells in a CGNP- like state. (C) M-Smo tumors showed increased Eomes, consistent with a greater fraction in a UBC-like state. (D) No significant differences in the fractions of cells expressing marker of the glutamatergic lineage (Ascl1, Pax2, Pax3) noted in G-Smo tumors versus M-Smo tumor.

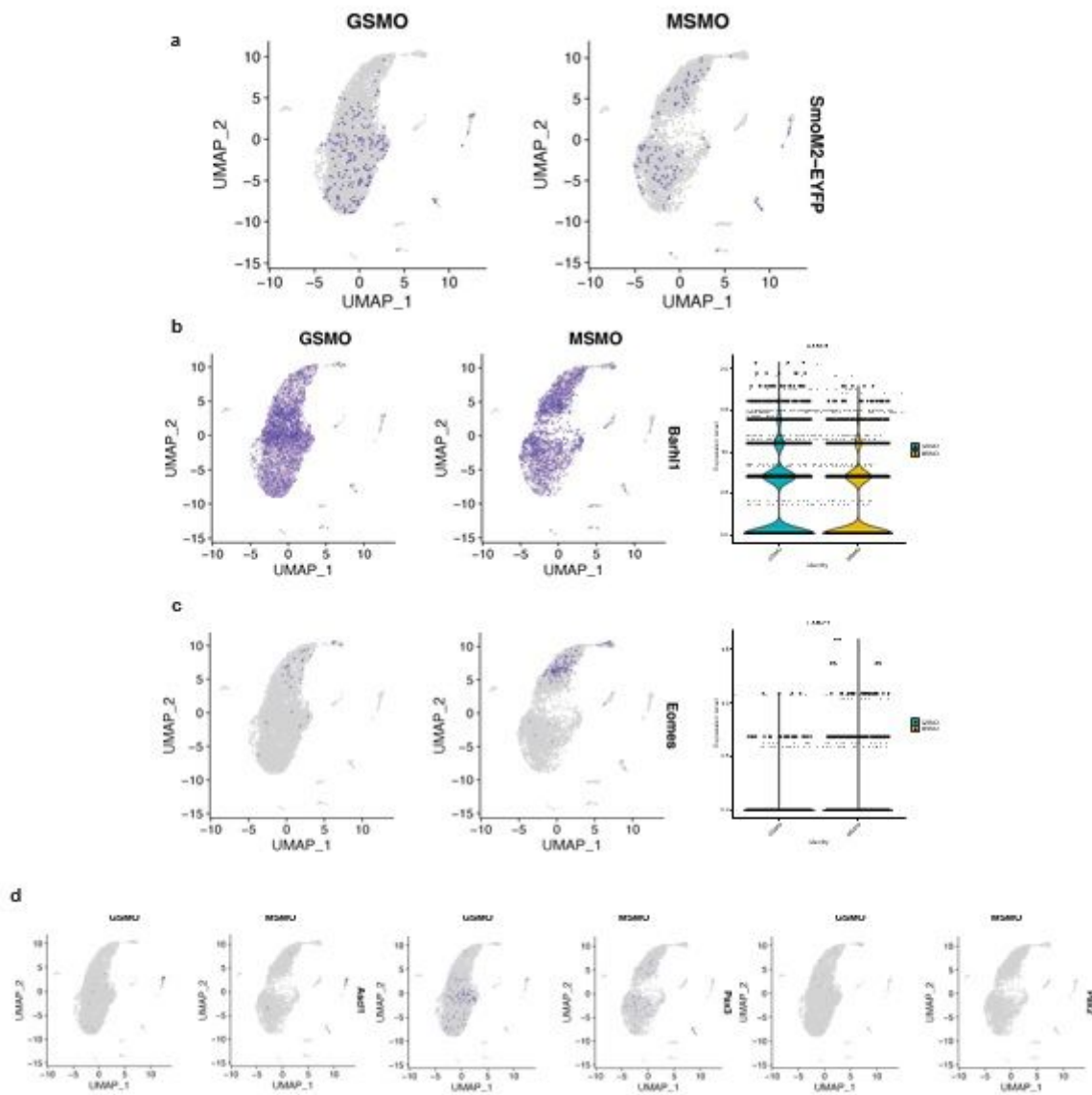


Figure 4

Similar range of cell fates in G-Smo and M-Smo tumors. Feature plots showing expression of the indicated lineage markers, color coded over the UMAP shown in (2D). (A) Yfp expression, denoting the SmoM2-activated lineage, was distributed similarly in both G-Smo and M-Smo tumors. Green circle shows oligodendrocytes; brown circle shows astrocytes. (B) G-Smo tumors showed increased Barhl1+ cells, consistent with a greater fraction of cells in a CGNP- like state. (C) M-Smo tumors showed increased Eomes, consistent with a greater fraction in a UBC-like state. (D) No significant differences in the fractions of cells expressing marker of the glutamatergic lineage (Ascl1, Pax2, Pax3) noted in G-Smo tumors versus M-Smo tumor.

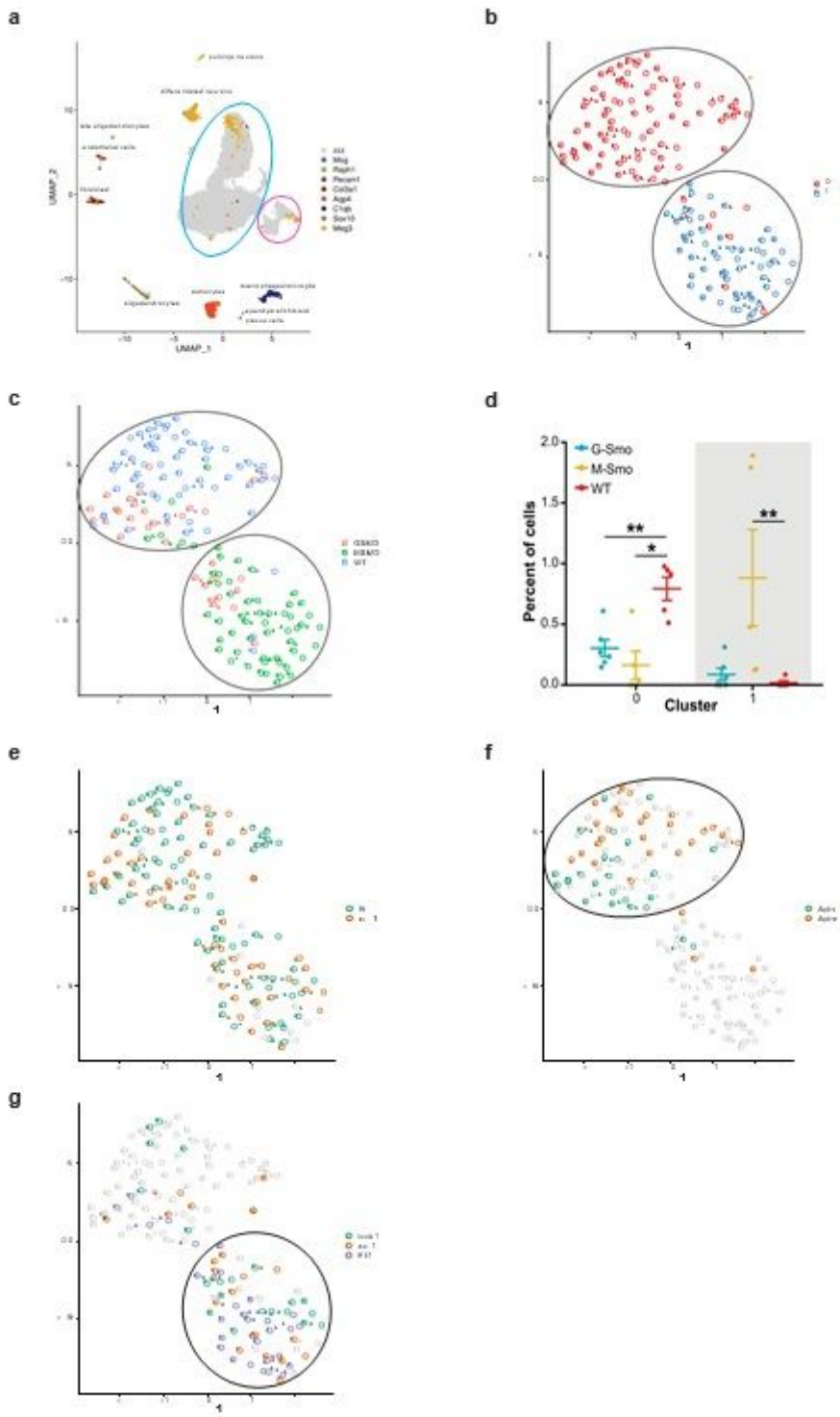


Figure 5

Tumor-specific gene expression in endothelial cells. (A) UMAP plot of cells from G-Smo and M-Smo tumors combined with cells from P7 WT cerebella, analyzed using the Harmony algorithm. The blue circle shows the region where neural-progenitor-like tumor cells and CGNPs localize. The pink circle shows the GABAergic interneuron lineage. Stromal cell types are identified by the expression of the indicated, color-coded markers. (B) UMAP showing endothelial cells from G-Smo, M-Smo and P7 WT, with clusters color-coded. (C) genotype color coded on the UMAP from (B). Circles indicate the positions of the clusters. (D)

Comparison of the indicated cluster populations in G-Smo, M-Smo and P7 WT. Dots represent values for individual replicates, bars indicate the means and whiskers indicate the SEM. (E-G) Feature plots on UMAP from (B), showing expression of (E) endothelial markers *Cldn5* and *Pecam1*, (F) Cluster E0 markers *Apln* and *Aplnr*, or (G) tumor-specific Cluster E1 markers *Abcb1a* (aka *Mdr1*), *Cxcl12* and *Flt1*.

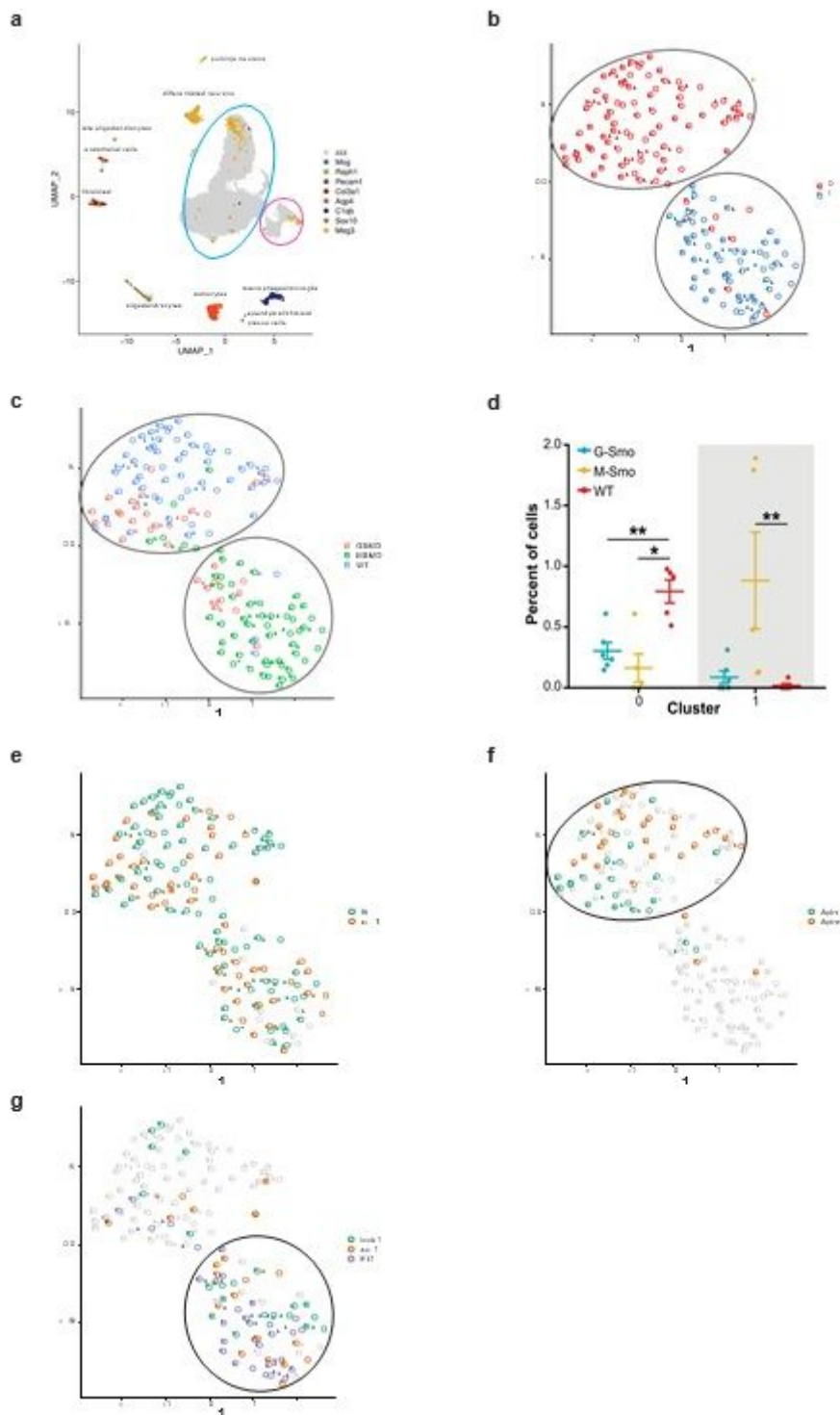


Figure 5

Tumor-specific gene expression in endothelial cells. (A) UMAP plot of cells from G- Smo and M-Smo tumors combined with cells from P7 WT cerebella, analyzed using the Harmony algorithm. The blue circle

shows the region where neural-progenitor-like tumor cells and CGNPs localize. The pink circle shows the GABAergic interneuron lineage. Stromal cell types are identified by the expression of the indicated, color-coded markers. (B) UMAP showing endothelial cells from G-Smo, M-Smo and P7 WT, with clusters color-coded. (C) genotype color coded on the UMAP from (B). Circles indicate the positions of the clusters. (D) Comparison of the indicated cluster populations in G-Smo, M-Smo and P7 WT. Dots represent values for individual replicates, bars indicate the means and whiskers indicate the SEM. (E-G) Feature plots on UMAP from (B), showing expression of (E) endothelial markers *Cldn5* and *Pecam1*, (F) Cluster E0 markers *Apln* and *Aplnr*, or (G) tumor-specific Cluster E1 markers *Abcb1a* (aka *Mdr1*), *Cxcl12* and *Flt1*.

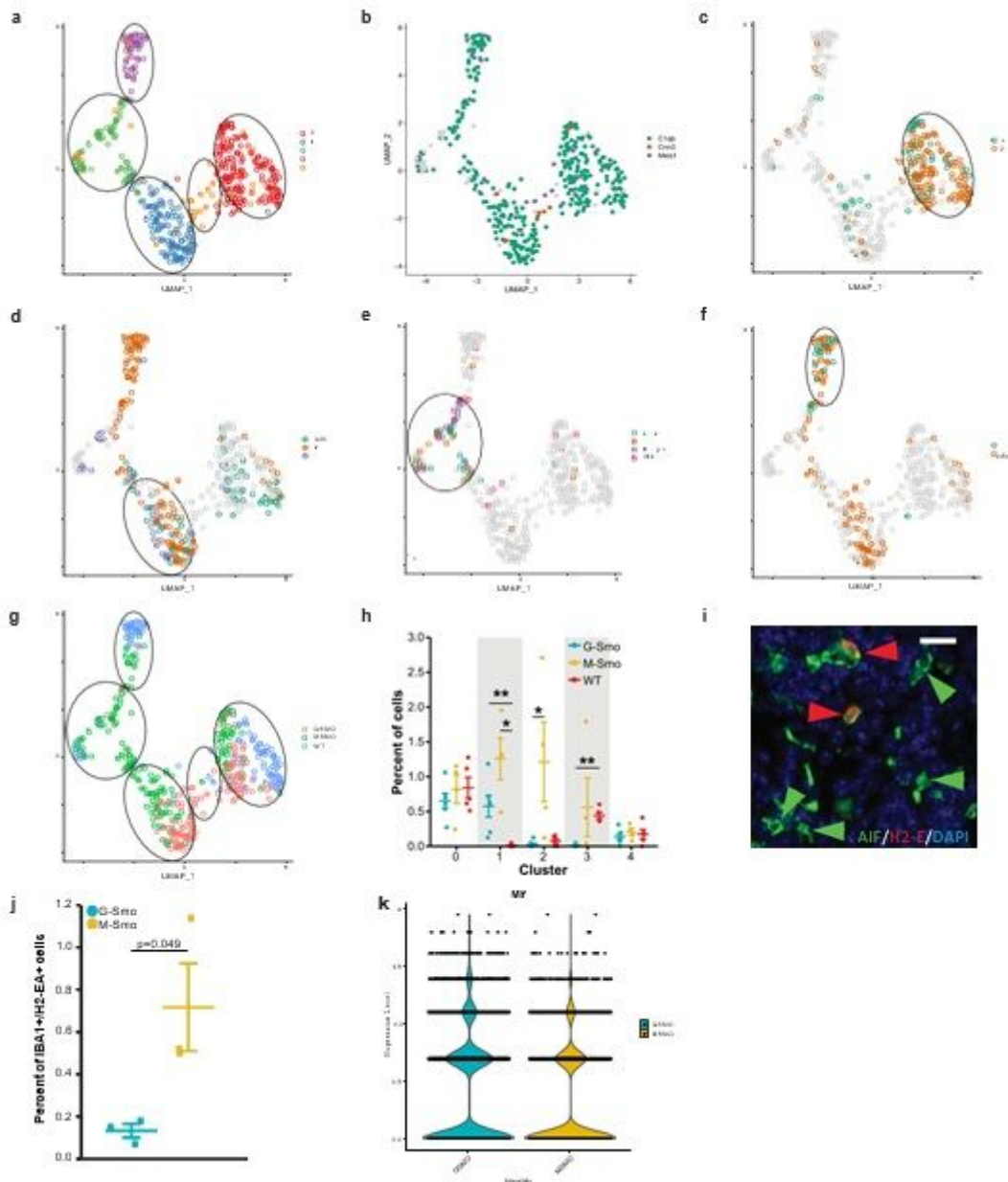


Figure 6

M-Smo tumors show macrophage and microglial populations not present in G-Smo tumors. (A) UMAP showing myeloid-like cells from G-Smo, M-Smo and P7 WT, with clusters color-coded and circled. (B)

Feature plot on UMAP from (A), showing expression of the pan-macrophage and microglial marker *C1qb* and the choroid plexus epithelial markers *Cnn3* and *Meis1*. Cluster 4 does not show *C1qb* expression. (C-F) Feature plots on UMAP from (A), showing expression of (C) Cluster M0 markers *Cx3cr1* and *Sparc*, (D) Cluster M1 markers *Igf1*, *Mrc1* and *wfdc17*, or (E) Cluster M2 markers *Ccr2*, *Cd74*, *H2-Ea-ps*, and *Il1b* (F) Cluster M3 markers *Mrc1* and *Cd163*. (G) genotype color coded on the UMAP from (A). Circles indicate the positions of the clusters. (H) Comparison of the indicated cluster populations in G-Smo, M-Smo and P7 WT. Dots represent values for individual replicates, bars indicate the means and whiskers indicate the SEM. (I) Immunohistochemistry for IBA1 (green) and H2-E (red) in a representative M-Smo section. Green arrowheads show examples of IBA1+/H2-E- cells. Red arrowheads highlight AIF+/H2-E+ cells. (J) Quantification of replicate sections stained as in (I), comparing the fractions of AIF+/H2-E+ cells in G-Smo and M-Smo tumors. (K) Violin plots showing the number of cells expressing the indicated level of *Mif* in each genotype.

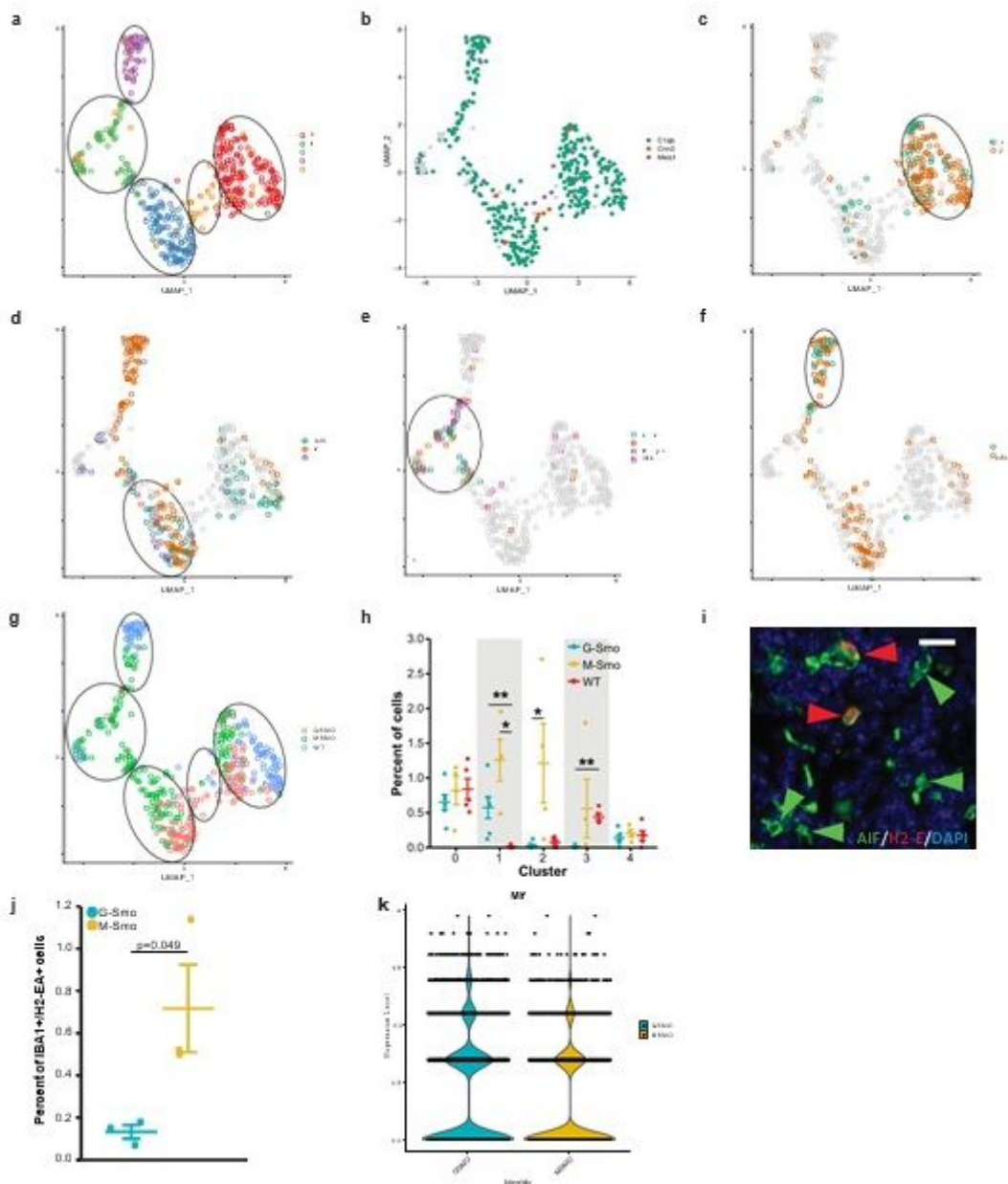


Figure 6

M-Smo tumors show macrophage and microglial populations not present in G-Smo tumors. (A) UMAP showing myeloid-like cells from G-Smo, M-Smo and P7 WT, with clusters color-coded and circled. (B) Feature plot on UMAP from (A), showing expression of the pan-macrophage and microglial marker *C1qb* and the choroid plexus epithelial markers *Cnn3* and *Meis1*. Cluster 4 does not show *C1qb* expression. (C-F) Feature plots on UMAP from (A), showing expression of (C) Cluster M0 markers *Cx3cr1* and *Sparc*, (D) Cluster M1 markers *Igf1*, *Mrc1* and *wfdc17*, or (E) Cluster M2 markers *Ccr2*, *Cd74*, *H2-Ea-ps*, and *Il1b* (F) Cluster M3 markers *Mrc1* and *Cd163*. (G) genotype color coded on the UMAP from (A). Circles indicate the positions of the clusters. (H) Comparison of the indicated cluster populations in G-Smo, M-Smo and P7 WT. Dots represent values for individual replicates, bars indicate the means and whiskers indicate the SEM. (I) Immunohistochemistry for IBA1 (green) and H2-E (red) in a representative M-Smo section. Green arrowheads show examples of IBA1⁺/H2-E⁻ cells. Red arrowheads highlight AIF⁺/H2-E⁺ cells. (J) Quantification of replicate sections stained as in (I), comparing the fractions of AIF⁺/H2-E⁺ cells in G-Smo and M-Smo tumors. (K) Violin plots showing the number of cells expressing the indicated level of *Mif* in each genotype.

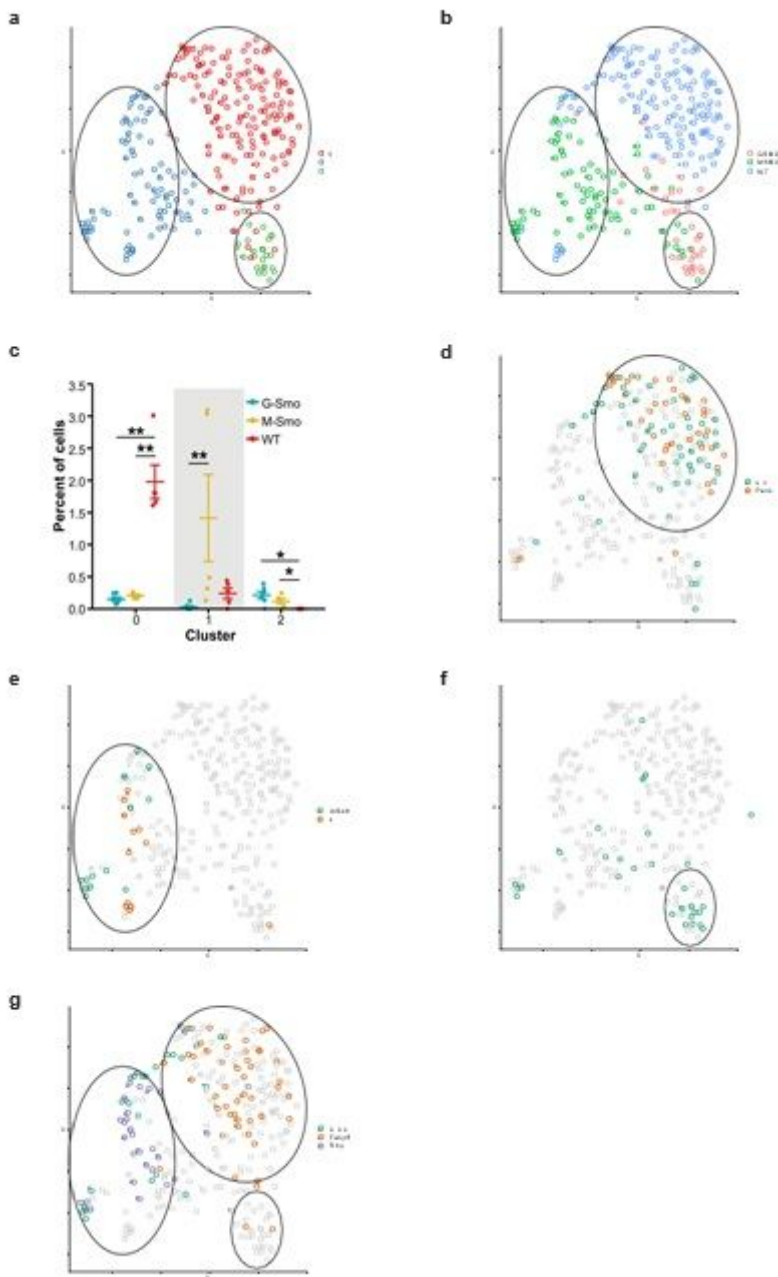


Figure 7

Different fibroblastic populations in G-Smo and M-Smo tumors. (A) UMAP showing fibroblastic cells from G-Smo, M-Smo and P7 WT, with clusters color-coded and circled. (B) genotype color coded on the UMAP from (A). Circles indicate the positions of the clusters. (C) Comparison of the indicated cluster populations in G-Smo, M-Smo and P7 WT. Dots represent values for individual replicates, bars indicate the means and whiskers indicate the SEM. (D-G) Feature plots on UMAP from (A), showing expression of (D) Cluster F0 markers Axin2 and Penk, (E) Cluster F1 markers Igfbp6 and Moxd1, (F) Cluster F2 marker Htra3, and (G) retinoic acid signaling components Crabp2, Fabp5 and Rbp4.

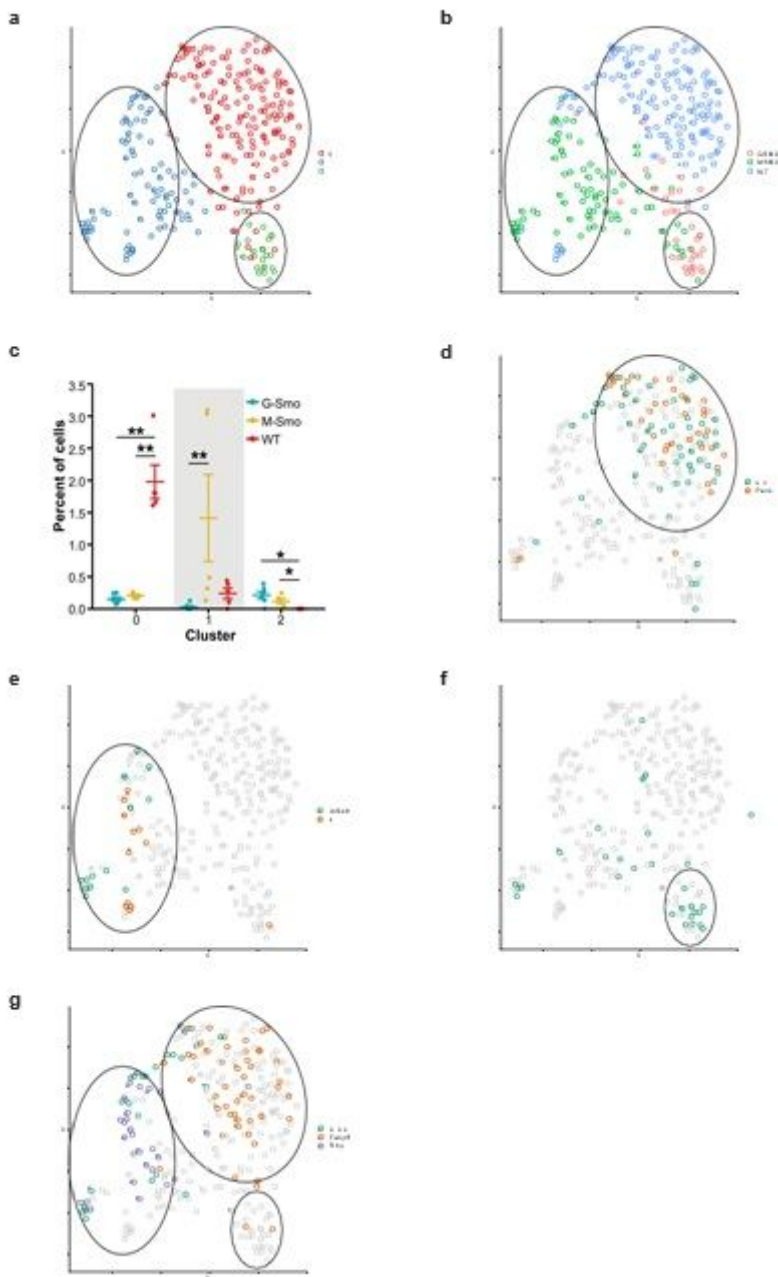


Figure 7

Different fibroblastic populations in G-Smo and M-Smo tumors. (A) UMAP showing fibroblastic cells from G-Smo, M-Smo and P7 WT, with clusters color-coded and circled. (B) genotype color coded on the UMAP from (A). Circles indicate the positions of the clusters. (C) Comparison of the indicated cluster populations in G-Smo, M-Smo and P7 WT. Dots represent values for individual replicates, bars indicate the means and whiskers indicate the SEM. (D-G) Feature plots on UMAP from (A), showing expression of (D) Cluster F0 markers Axin2 and Penk, (E) Cluster F1 markers Igfbp6 and Moxd1, (F) Cluster F2 marker Htra3, and (G) retinoic acid signaling components Crabp2, Fabp5 and Rbp4.

Supplementary Files

This is a list of supplementary files associated with this preprint. Click to download.

- [supptable1microarrayGSMOvsMSMOgershon.pdf](#)
- [supplement1.pdf](#)
- [supplement2.pdf](#)
- [supptable2microarrayGSMOvsMSMOschuller.pdf](#)
- [supplement3.csv](#)
- [supptable3clustermarkersGM.csv](#)
- [supplement4.csv](#)
- [supptable4GSMO127vtumorMSMO.csv](#)
- [supptable5clustermarkersGMWT.csv](#)
- [supplement5.csv](#)
- [supplement6.csv](#)
- [supptable6clustermarkersendothelial.csv](#)
- [supplement7.csv](#)
- [supptable7clustermarkersmyeloid.csv](#)
- [supplement8.csv](#)
- [supptable8clustermarkersfibroblast.csv](#)
- [supplement9.pdf](#)
- [SupplementaryFig1.pdf](#)